The University of California
Santa Cruz

# Pulsed Nuclear Magnetic Resonance Imaging

A Thesis submitted in partial satisfaction of
the requirements for the degree of

BACHELOR OF ARTS
in
PHYSICS

by

Jonathan W. Loughboro

April, 1986

The Thesis of J.W. Loughboro
is approved by:

F. Bridges / CAH.
Technical Advisor - Frank Bridges

Chairman, Board of Studies -
Michael Nauenberg

Thesis Supervisor - Clemens Heusch

## ABSTRACT

A new technique of creating planar images of cross-sectional human tissue, for diagnostic medicine, using nuclear magnetic resonance is described. Five magnetic fields are used with a Fourier transform technique to obtain images which show the concentration of $^{1}H$ nuclei (in water, fats, and oils) contained in the tissue of the organism. The method consists of applying a sequence of short rf pulses timed with a particular sequence of three gradient field pulses to a sample within a large static field of 1.5 Tesla. By Fourier transforming the response of the system and using a digital image processing computer, the images are created as negatives. Also presented is the original imaging method which constructs images from projections using a computer algorithm. In conclusion to the description of the imaging process, a discussion of whole-body instrumentation is given. In preparation for the discussion of the imaging techniques, the principles of nuclear magnetic resonance are introduced, using quantum mechanics to describe the geometry of an isolated spin in a static field. Statistical mechanics are used to describe the relative intensity of the magnetization of the sample in thermal equilibrium. Finally, the classical Bloch equations are solved to describe the time-dependent behavior of the sample magnetization vector following an rf pulse.

CONTENTS:

## I. Introduction

Nuclear magnetic resonance (NMR) imaging is a technique which creates planar sections of biological tissue to be viewed as an x-ray negative is viewed, however, NMR imaging uses only magnetic fields and is harmless biologically. Figures (A-C), which appear in sec. X, show images [1] produced by this technique. They were produced with the latest technology. In fact, nuclear magnetic resonance imaging is barely over a decade old.

In this paper, we will describe how the images of figs.(A-C) were created. Also, we will treat some of the underlying difficulties in creating the images and digress into areas of nuclear magnetic resonance that are important to imaging. In order to understand the imaging process, a fairly thorough understanding of nuclear magnetic resonance is necessary.

In 1946, two independent groups simultaneously devised the technique of nuclear magnetic resonance. The groups were the Purcell and Pound group at Harvard [2] and the Bloch and Hansen group at Stanford [3].

In brief, nuclear magnetic resonance is produced as follows. By placing nuclei of non-zero spin in a static magnetic field, a precession of the nucleus is induced. By applying an alternating magnetic field at a frequency equal to the precession frequency of the nucleus and perpendicular to the static field, the precessing nucleus is forced to resonate. If a sample of nuclei is resonated with the alternating magnetic field, the sample will

re-emit some of its absorbed energy. This emission signal contains all the information about the sample.

In order to create an image, linear magnetic field gradients are used to spatially encode the signal emitted from the sample, such that it can be used to create an image of the distribution of nuclei in the sample. This will be treated in full in the final section.

In the next two sections, we discuss the effects of NMR from the viewpoint of single nuclei, highlighting the concepts of imaging where necessary. Then, in the following two sections, NMR is treated from a macroscopic (sample) viewpoint, which also gives relevant information on imaging. Finally, in section VI, the process of imaging is treated using the concepts developed in the sections preceding it. We begin now with some physical principles of the nucleus, discuss the molecules relevant to imaging and how nuclei are resonated in practice.

## II. Physical Principles

In the early 1920s, Stern and Gerlach conducted molecular beam experiments (deflection of atoms and particles in space by a field gradient) which provided much information about nuclear spins and magnetic moments.

The intrinsic angular momentum (spin) of a nucleus corresponds to a current flowing around the axis of rotation, which generates a small magnetic field. Each nucleus of non-zero spin (those nuclei whose protons and neutrons do not cancel in pairs) has a net magnetic moment proportional to the intrinsic angular momentum $\vec{J}$ by $\vec{\mu} = \gamma \vec{J}$, where $\gamma$ is the constant called the gyromagnetic ratio.

Classically, a nucleus will precess when placed in a static magnetic field of intensity $H_o$ at an angular frequency $\omega_p = \gamma H_o$ called the Larmor precession frequency.

By perturbing the precessing moment with a radio frequency field of intensity $H_1$ and frequency $\omega_o$, equal to $\omega_p$, at right angles to the static field $H_o$, the moment resonates. Figure (1) shows an experimental set-up to observe magnetic resonance in the laboratory [4]. The coherent precession of the magnetic moments within the sample induces an alternating current in the pick-up coil, via Lenz's law, which provides all the information about the sample.

BIOLOGICAL TISSUE CHARACTERISTICS:

The $^{1}H$ nucleus is the source of signal emission used by imagers since it has a large magnetic moment and is found in high concentrations distributed widely in the body.

We are concerned here with the biological tissue of the human organism, however, images of other animals and plants can be made as well. Human tissue contains roughly 75% water on average [5]. Different tissues contain different concentrations of $H_2O$. Also, lipids (fats), and oils contain $^{1}H$ nuclei and are spatially distributed throughout the body.

In addition to protons, other NMR-sensitive nuclei are $^{13}C$, $^{19}F$, $^{23}Na$, $^{31}P$, and $^{39}K$ [6]. These nuclei are difficult to use in imaging since they are smaller in concentration and are lower in inherent NMR-sensitivity than $^{1}H$.

The intensity of the NMR signal emitted from a local region of tissue is directly proportional to the spin density there. By spin density, we imply the concentration of $^{1}H$ nuclei in water, fat, and oils distributed throughout the sample. We will return to spin-density of $^{1}H$ nuclei in sec.(VI) on imaging after we have presented some basic concepts of NMR.

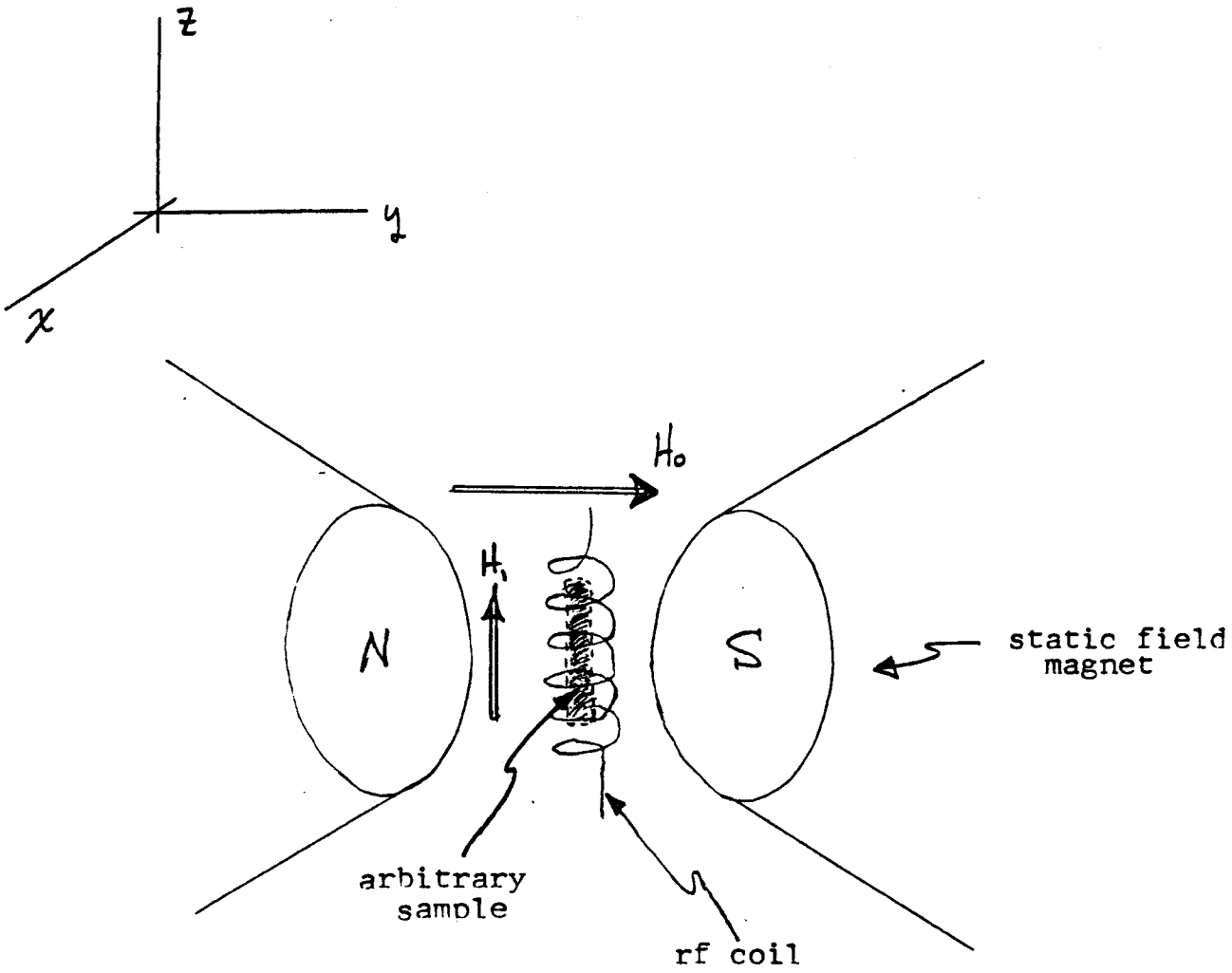


Fig. 1. Experimental set-up for creating magnetic resonance in the laboratory. The sample nuclei precess when placed in the large static field magnet. They are then resonated by the perpendicular rf field $H_1$ which is applied at the precession frequency.

## III. A Spin in a Static Magnetic Field

In what follows, we will consider an isolated magnetic system in an external magnetic field to better acquaint ourselves with the phenomenon of nuclear magnetic resonance. First, we examine the energy states of a nucleus in an external magnetic field.

### THE HAMILTONIAN:

In general, nuclei contain protons and neutrons which may be in orbit-like motions while at the same time having an intrinsic spin. For a hydrogen nucleus, it is the proton's motion which creates a total angular momentum $\vec{J}$ and total magnetic moment $\vec{\mu}$: which are parallel and described by [7]

$$\vec{\mu} = g\left(\frac{q_e}{2M_p}\right)\vec{J}. \qquad (1)$$

$M_p$ is the proton's mass, and g, called the "nuclear g-factor," is a number usually near 1 but equal to about 5.6 for a pure spin. From eq.(1), the gyromagnetic ratio $\gamma$ for a given atomic species is approximated by $g(q_e/2M_p)$. (In practice, it is determined experimentally.)

In quantum mechanical operator notation, $\hat{\mu} = \gamma\hat{J}$. Upon application of $H_o$, a nucleus experiences an interaction energy

$-\mu \cdot H_o$, yielding the simple Hamiltonian $\hat{\mathcal{H}} = -\vec{\mu} \cdot \vec{H}_o$. If, for simplicity, we apply $\vec{H}_o$ along the z-axis, the component of $\hat{J}$ "parallel" to $\vec{H}_o$ is $\hat{J}_z$. Therefore,

$$\hat{\mathcal{H}} = -\gamma H_o \hat{J}_z . \qquad (2)$$

The three spatial parts of angular momentum, $\hat{J}_x$, $\hat{J}_y$, and $\hat{J}_z$, form a set of noncommuting Hermitian operators which together define $\hat{J}^2 = \hat{J}_x^2 + \hat{J}_y^2 + \hat{J}_z^2$. The compatibility between $\hat{J}^2$ and the components of the total angular momentum $\hat{J}$ provides the eigenvalue equations $\hat{J}^2\phi = \alpha\phi$ and $\hat{J}_z\phi = \beta\phi$ with the set of simultaneous eigenfunctions $\phi$. The respective eigenvalues of $\hat{J}^2$ and $\hat{J}_z$ are $\alpha = j(j+1)\hbar^2$ and $\beta = m\hbar$, where j is the total spin quantum number with eigenstates m. (j and m are related by $-j \leq m \leq j$.)

The eigenvalues of the Hamiltonian of eq.(2) are multiples ($\gamma H_o$) of the eigenvalues of $\hat{J}_z$, from which we find the allowed energy eigenvalues, (also called the nuclear Zeeman levels) [8]

$$E_m = -\gamma\hbar H_o m \quad , \quad m = j, j-1, \cdots, -j. \qquad (3)$$

These are illustrated in fig.(2) for j=3/2 (e.g. nuclei of $B^{11}$ and $Na^{23}$ [9]).

If we now apply a resonant rf pulse magnetic field $H_1$ across the sample, it causes transitions between levels of energy $\Delta E = \gamma\hbar H_o$. A current in the RF coil is observed following $H_1$ as a large number of nuclei drop back to their lower energy states emitting energy $\hbar\omega_o$. Therefore, the resonance condition is

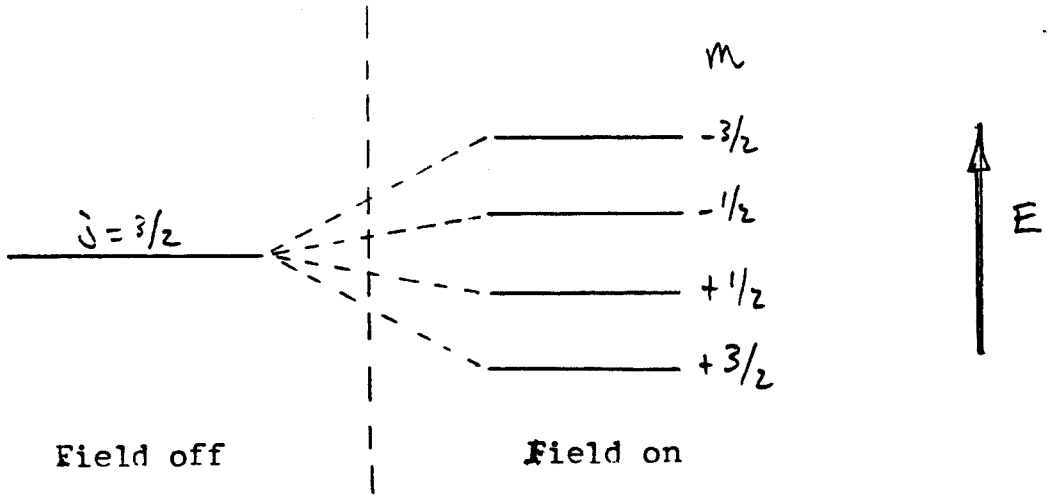


Fig. 2. Simple diagram of nondegenerate Zeeman eigenstates m for a single spin 3/2 system.

$\omega_o = \Delta E/\hbar$ or, $\omega_o = \gamma H_o$. The proton nucleus, the nucleus of importance in imaging, has energy $4.2 \times 10^{-8}$ ev in a static field of 1.5 Tesla (=15KG) producing photon absorption and emission at $\nu = 10.1$ MHz.

GEOMETRICAL DESCRIPTION:

The geometrical behavior of a spin in a static magnetic field can be seen by considering the components of the magnetic moment $\hat{\mu}$ of a single spin as it interacts with the field $H_o$, in which case

$$\langle \hat{\mu}(t) \rangle \equiv \hat{i} \langle \hat{\mu}_x(t) \rangle + \hat{j} \langle \hat{\mu}_y(t) \rangle + \hat{k} \langle \hat{\mu}_z(t) \rangle . \qquad (4)$$

The terms $\hat{i}$, $\hat{j}$ and $\hat{k}$ are the unit basis vectors of the Cartesian system and <...> denotes the expectation value, (the probability of an observable having a particular result).

From Appendix A, the components in eq.(4) for the spin-1/2 proton nucleus are [10]

$$\langle \hat{\mu}_x(t) \rangle = \gamma\hbar ab\cos(\alpha - \beta + \omega_o t), \qquad (5)$$

$$\langle \hat{\mu}_y(t) \rangle = -\gamma\hbar ab\sin(\alpha - \beta + \omega_o t), \quad \text{and} \qquad (6)$$

$$\langle \hat{\mu}_z \rangle = (\gamma\hbar/2)[a - b], \qquad (7)$$

where a and b are real, positive constants and $\alpha$ and $\beta$ are real but may be positive or negative. These equations show that

$\langle\hat{\mu}_x(t)\rangle$ and $\langle\hat{\mu}_y(t)\rangle$ oscillate with the Larmor precession frequency $\omega_o$ while $\langle\hat{\mu}_z\rangle$ is independent of time. Also, the amplitudes of eqs.(5 & 6) are equal. With these points in mind, and the fact that $\langle\hat{\mu}_x(t)\rangle^2 + \langle\hat{\mu}_y(t)\rangle^2$ is constant, we may interpret the magnetic moment $\hat{\mu}$ in eq.(4) as a vector which precesses in the x-y plane making a fixed angle $\lambda$ with the z-axis in fig.(3). (The axes x', y' and z' rotate with the laboratory frame x, y and z at angular frequency $\omega_o$ ).

In classical precession the motion of each component of angular momentum is completely determined, whereas in quantum mechanics only one spin component is ever determined by measurement. Therefore, fig.(3) at best should be considered a cone defined by the precession of $\hat{\mu}$ whose tip is at the origin; $\langle\hat{\mu}_x(t)\rangle$ and $\langle\hat{\mu}_y(t)\rangle$ are uncertain while $\langle\hat{\mu}_z\rangle$ is determined, (See ref.[11]).

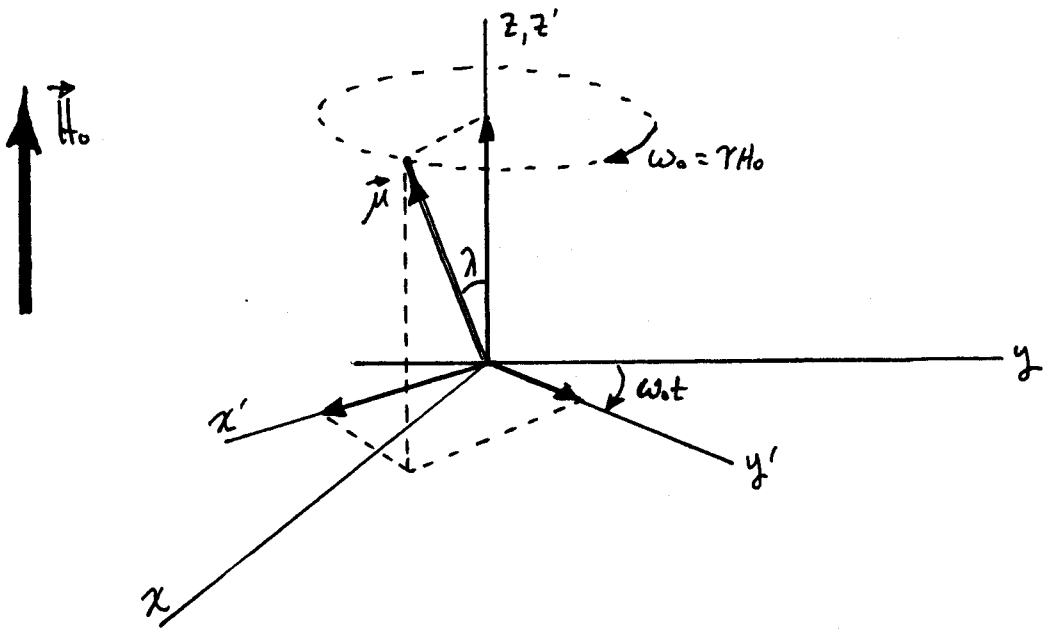


fig.(3)

## IV. Thermal Equilibrium Populations

In a biological sample, with many $^1H$ nuclei (spin-1/2), we label two populations corresponding to the two (=2j+1) eigenstates m. To these populations, we assign occupation numbers $N_+$ and $N_-$ corresponding to m=+1/2 and m=-1/2 respectively, where the total population $N = N_+ + N_-$. The net magnetic moment per unit volume, or magnetization $\vec{M}$, arises from a greater number of spins "aligned" with the field $\vec{H}_o$. (Again, it is the component $\hat{J}_z$ that is said to be "parallel" or "antiparallel" with $\vec{H}_o$). Therefore, we have the population difference $n = N_+ - N_- > 0$ following the application of $H_o$. The foregoing is summarized in fig.(4) and depicts the nuclear Zeeman effect for a sample of N protons in an arbitrary sample.

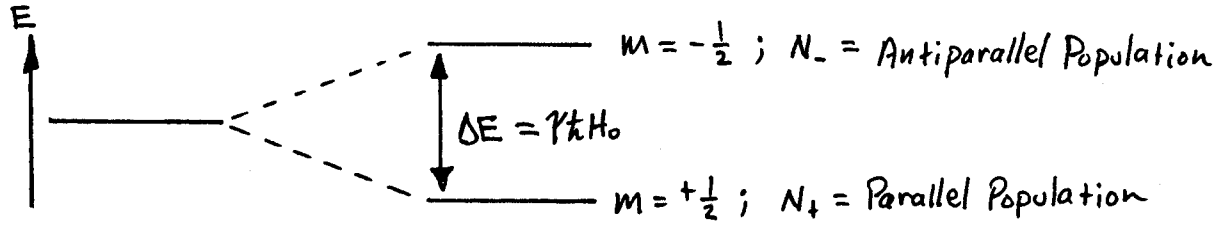


fig.(4)

We use the Boltzmann distribution to calculate the 'strength' of the magnetization in areas of tissue that are high in hydrogen content. The expression

$$N(m) = \frac{N\exp(-E_m/kT)}{\sum_{-1/2}^{1/2} \exp(-E_m/kT)}, \qquad (1)$$

gives the equilibrium population where $E_m = -\gamma\hbar H_o m$ for each of the $M = \pm 1/2$ eigenstates; k is the Boltzmann constant and T is the temperature of the spin system. The denominator is the normalizing factor called the partition function, which, for simplicity, can be expanded in the high temperature limit ($\gamma\hbar H_o m / KT << 1$) to yield [12]

$$\sum_{m=-1/2}^{m=1/2} \exp\left[\frac{-\gamma\hbar H_o m}{kT}\right] = (2(\tfrac{1}{2})+1) - \frac{\gamma\hbar H_o}{kT}\sum_{-1/2}^{1/2} m + \frac{1}{2}\left(\frac{\gamma\hbar H_o}{kT}\right)^2 \sum_{-1/2}^{1/2} m^2 + \cdots$$

The second term in the expansion is zero since $\sum_{-1/2}^{1/2} m = 0$, and higher order terms approach zero for $\gamma\hbar H_o/kT << 1$. Therefore, eq.(1) can be approximated by

$$N(m) = \frac{N}{2}\exp\left(\frac{+\gamma\hbar H_o}{2kT}\right). \qquad (2)$$

Again, we define the population difference $n = N_+ - N_-$, which is the excess number of nuclei in the lower energy state (those nuclei that contribute to the magnetization of the sample).

Therefore,

$$n = N_+ - N_- = \frac{N}{2}\left[\exp\left(\frac{\gamma\hbar H_o}{2KT}\right) - \exp\left(-\frac{\gamma\hbar H_o}{2KT}\right)\right]$$

$$\simeq N \sinh\left(\frac{\gamma\hbar H_o}{2KT}\right). \qquad (3)$$

This can be simplified since $\sinh(\gamma\hbar H_o/2KT) \simeq (\gamma\hbar H_o/2KT)$ in the high temperature limit, ($T \simeq 310K$ body temperature). When normalized, eq.(3) becomes

$$\frac{n}{N} = \frac{\gamma\hbar H_o}{2KT}. \qquad (4)$$

At body temperature, in the large static field of 1.5 Tesla, eq.(4) gives roughly $8 \times 10^{-7}$ for $^1H$ nuclei. In other words, roughly 8 protons in $10^7$ will align with $H_o$ to contribute to the magnetization. This will give a relatively weak emission signal following resonance: an unfortunate fact for imaging since a weak signal requires lengthy imaging times.

## V. Resonance Theory

In order to understand the imaging technique used in figs.(A-C), we give in the following five sub-sections, an account of magnetic resonance from the viewpoint of the magnetization vector $\vec{M}$ in a given, homogeneous, volume element containing $^1H$ nuclei.

### MAGNETIC RESONANCE AS FORCED PRECESSION:

In 1950, Erwin L. Hahn published his now famous paper, Spin Echos [13], where he showed in detail the effects of nuclear induction due to free Larmor precession. The effect of the rf magnetic field pulse $H_1$ upon the established magnetization vector $\vec{M}$, initially at rest and parallel to $\vec{H}_o$, is shown in fig.(5) where resonance flips it into the x-y plane of the laboratory.

For convenience, we use the rotating frame of reference precessing at the Larmor frequency $\omega_o$. In this frame, $\vec{M}$ will no longer precess about the z-axis, but will appear stationary. Application of $H_1$ induces resonance where $\vec{M}$ rotates about $H_1$ with angular velocity $\gamma H_1$ in fig.(6): x', y', and z' the axes of the rotating frame. If $H_1$ is applied at resonance for a time $t_w$, the magnetization vector will rotate through an angle $\gamma H_1 t_w$, assuming $H_1$ is turned on and off infinitely fast. A pulse of

sufficient amplitude and duration can produce a rotation of any desired angle. In imaging, pulses producing 90° and 180° rotations are of importance, with lengths $t_w = \pi/2\gamma H_1$ and $\pi/\gamma H_1$ respectively.

RELAXATION:

The behavior of $\vec{M}$ before, during, and following a pulse is affected in several ways by weak interactions that cause relaxation [14].

We defined the parameter n in the last section as the difference between each population of spin-1/2 nuclei, manifested by the static field $H_o$. Therefore, a net number, n, of nuclei become aligned with $H_o$ creating a net magnetization $\vec{M}$ parallel to $\vec{H}_o$. This alignment is not instantaneous but occurs over several multiples of the spin-lattice relaxation time, $T_1$, associated with the coupling between the spin system and lattice. In general, experiments show that $T_1$ varies between roughly $10^{-5}$ and $10^{5}$ seconds for different samples [15]. Spin-lattice relaxation follows perturbations in the magnetic field, which include the application of $H_o$, shutting $H_o$ off, and applying $H_1$ with $H_o$ on.

A second relaxation phenomenon occurs between the spins themselves, called spin-spin relaxation. Following a perturbation in the magnetic field, spin-spin coupling allows heat to

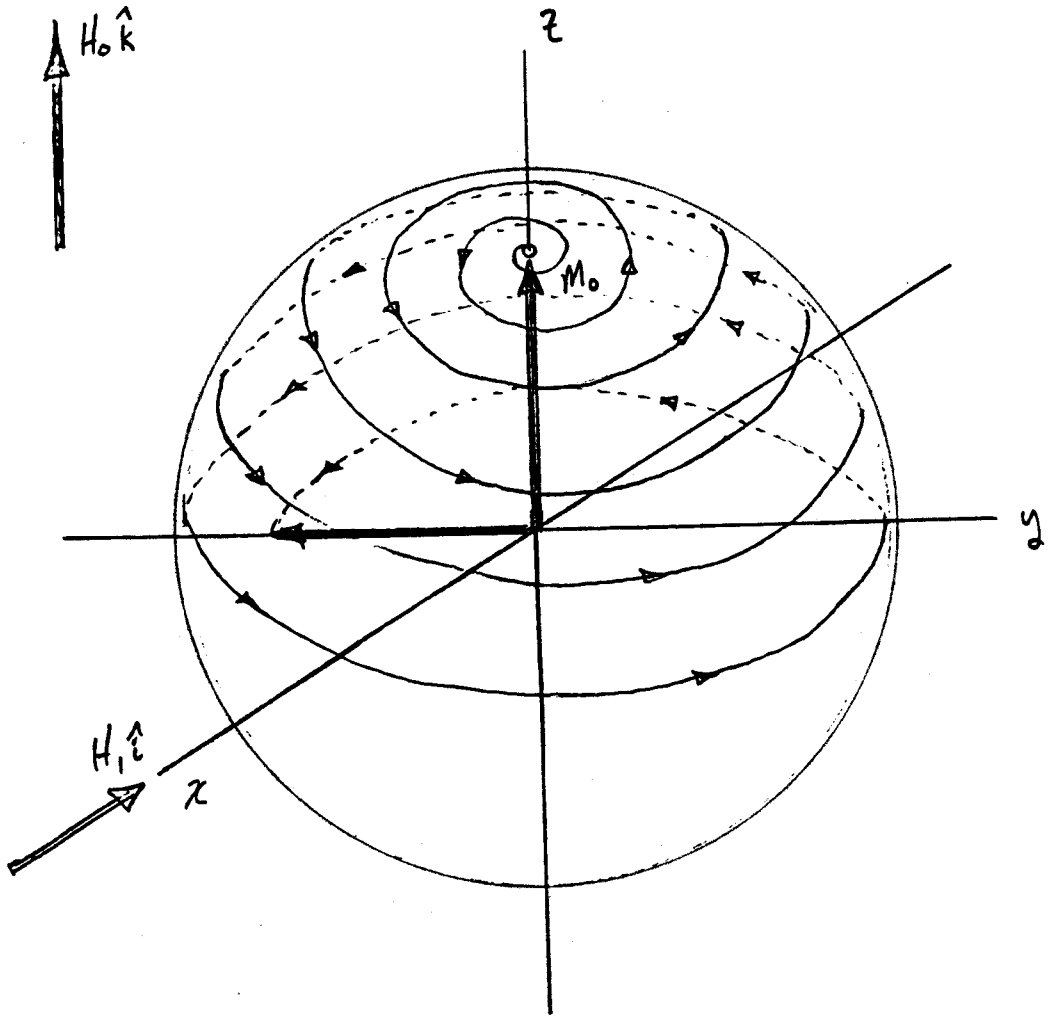


Fig. 5. Precession of magnetization viewed in the laboratory frame.

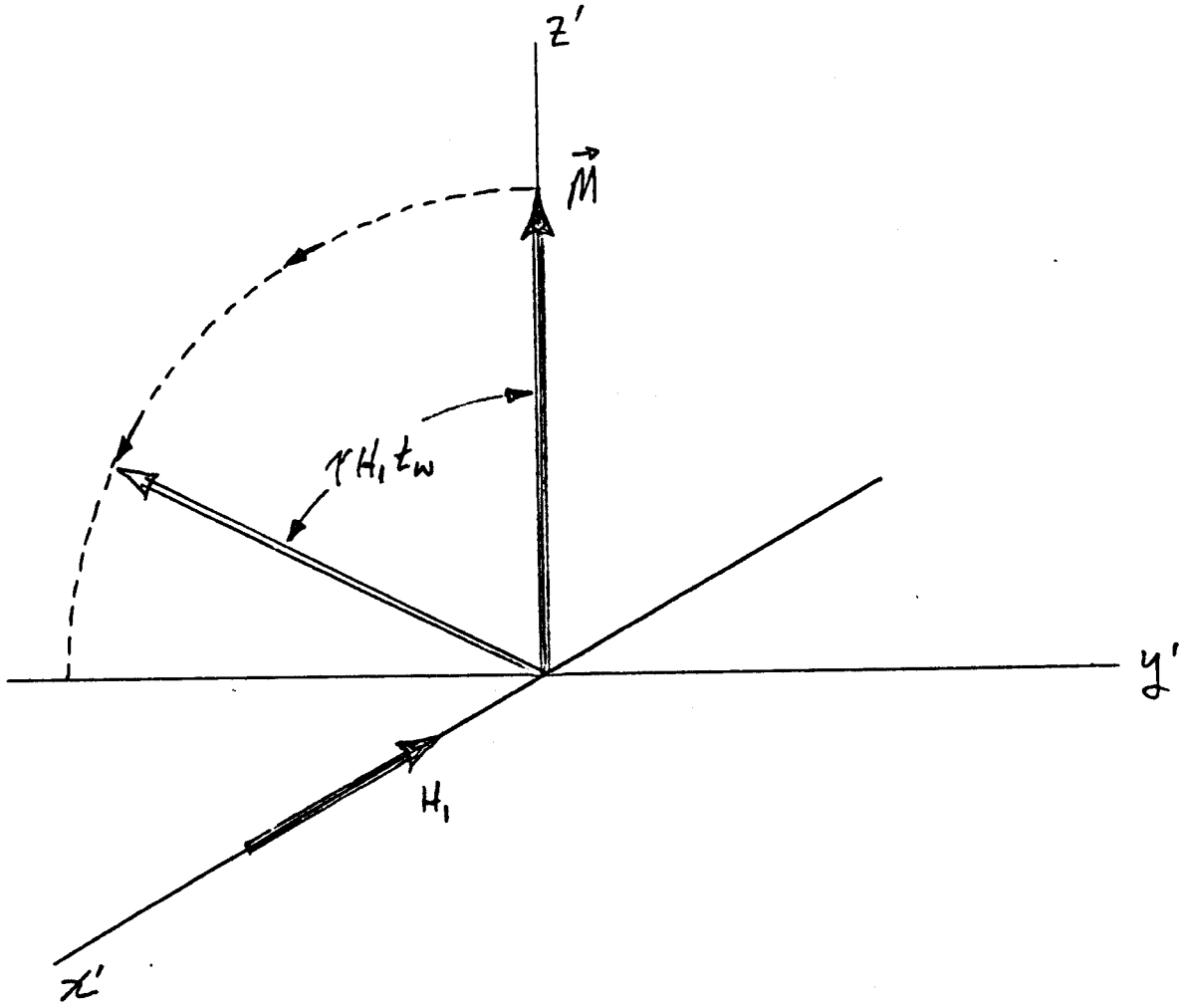


Fig. 6. Magnetization in the rotating frame during a 90° pulse.

transfer within the spin population exchanging no energy with the lattice.

We can summarize the relaxation process following the resonant 90° pulse by considering a group of spins precessing at their Larmor frequencies as follows. First, energy will be transferred in part to neighboring spins in a time $\sim T_2$, where mutual spin-spin flipping manifests a spin-temperature gradient. In this case, $T_2$ is called the spin-spin or transverse relaxation time, (transverse because $\vec{M}$ decays in the x'-y' plane). Second, part of this energy will be transferred to the lattice as thermal energy in a time $\sim T_1$ called the spin-lattice or longitudinal relaxation time, (longitudinal implying a realignment of $\vec{M}$ with the field $H_o$).

DECAY OF THE MAGNETIZATION VECTOR:

Once $\vec{M}$ has reached the x-y plane, it begins to decay by several mechanisms, one of which involves the inhomogeneity of the static magnetic field $H_o$. In practice, $H_o$ is never perfectly homogeneous across the sample. Variations in local magnetic fields produced by the static components of neighboring magnetic dipoles also contribute to the inhomogeneity. Therefore, one may assign to each volume element a magnetization vector $m_i$ (called an isochromat) where all moments within that volume element precess with the same constant Larmor frequency.

Initially, the transverse magnetization decays by mechanisms that are $T_2$ dependent. Therefore, we must insure that $t_w << T_2$, otherwise $\vec{M}$ would decay (partially or fully) before it reached its desired position. Experimentally, $H_1$ is made intense enough (>200 G) to maintain phase coherence between each $m_i$ during the pulse duration.

Once $\vec{M}$ has reached its desired position (the x'-y' plane for example) and $H_1$ is shut off, each isochromat vector $m_i$ will precess freely at its natural Larmor frequency, $\omega_i$. Since the isochromats vary in frequency, they will dephase, or fanout, in the x'-y' plane as illustrated in fig.(7). Parts A through D show the effects of fanout following the resonant rf pulse. And, parts E and F show the effects of spin-lattice relaxation where the magnetization regrows along the z'-axis from re-establishment of thermal equilibrium with $H_o$, (undetected by the coil, which lies in the x-y plane of the laboratory parallel to the y-axis).

In the pickup coil, the alternating magnetization will induce an rf current in precise analogy with an electric generator. But since $\vec{M}$ decays while in free precession, it produces the free induction decay (FID) signal appearing in fig.(8) with decay constant $T_2^*$ (to be defined shortly).

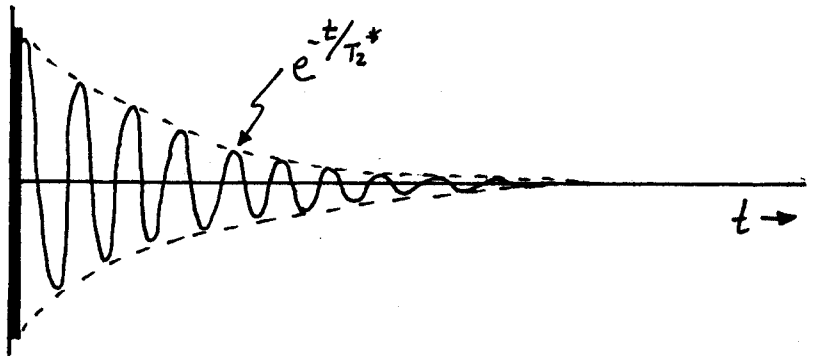


fig.(8)

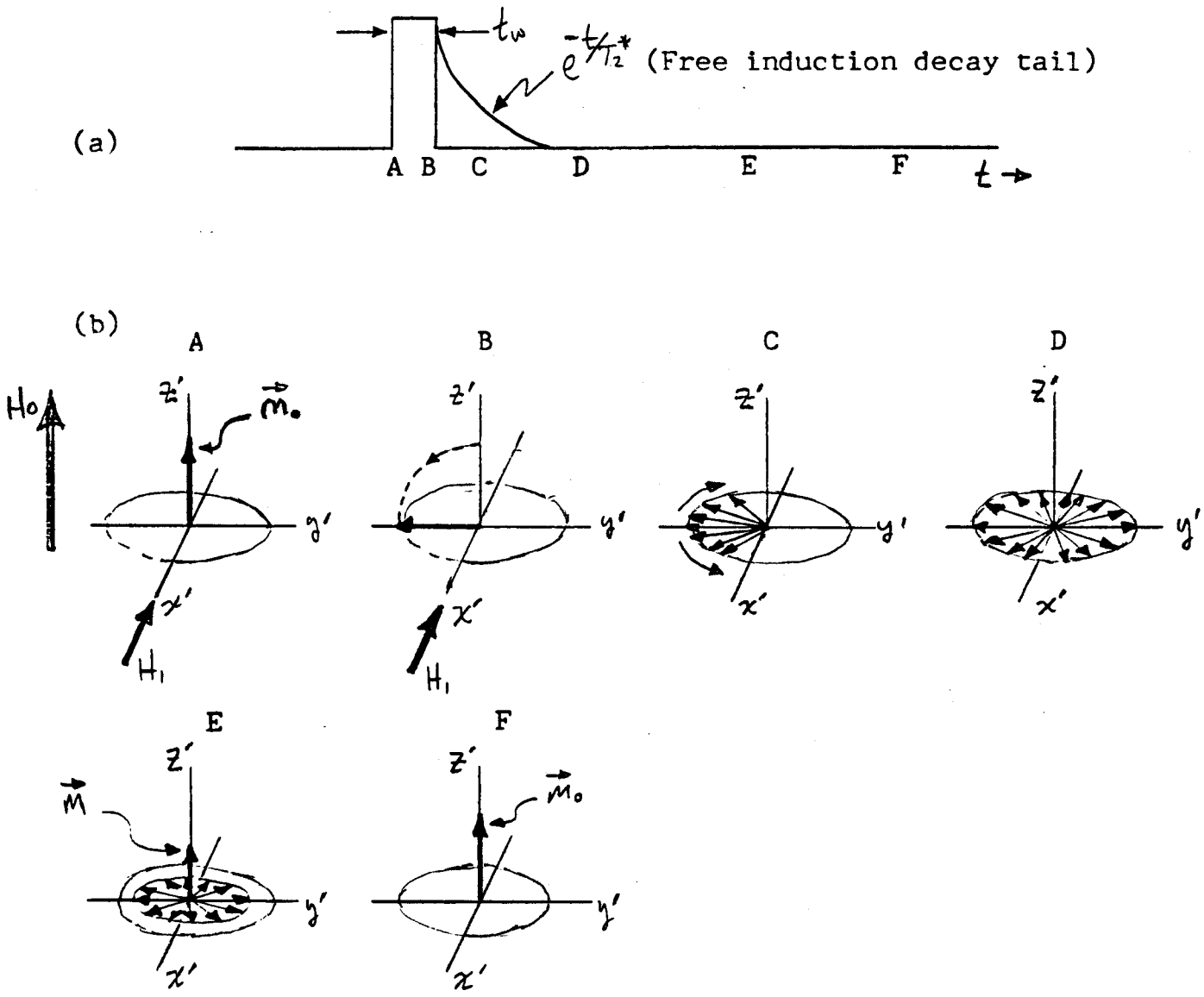


Fig. 7. Fanout of isochromats in the rotating frame, (a) 90° rf pulse in the time domain, (b) $H_1$ remains on only between A and B. Fanout occurs immediately following $H_1$; C to E. In F, the system has reached equilibrium again.

The distribution of frequencies among the isochromat population is typically a Gaussian or Lorentzian [16], and is given by $\Delta\omega = \gamma \Delta H_o$, $\Delta H_o$ being the inhomogeneity in $H_o$ across the sample. Therefore, a good measure of the fanout time due to $\Delta H_o$ is $\sim 1/\gamma \Delta H_o$.

Combining the effects of spin-spin relaxation and magnetic field inhomogeneities on fanout in the x'-y' plane, we arrive at the time constant describing the free induction decay tail in fig.(7) (parts B-D) by

$$\frac{1}{T_2^*} = \frac{1}{T_2} + \gamma \Delta H_o \,. \qquad (1)$$

Also, $T_2^*$ provides a parameter for measuring phase coherence of those spins contributing to $M_x$ and $M_y$ at any time t. It is essential in high-resolution imaging that $\Delta H_o$ be maintained small so that $T_2^*$ is very near $T_2$.

SPIN ECHOS:

All the isochromat moment vectors are assumed to be coherently in-phase upon reaching the x'-y' plane following the 90° pulse. Consequently, they will have definite phase relations for all time following the pulse, until relaxation has destroyed the phase memory. Therefore, at the time fanout has become random, each vector's position is determined by its past history. At a time $t = \tau$ after point B in fig.(9), flipping the plane of

vectors through 180° has a similar effect to that of time reversal. As the vectors travel in the same direction that they did before the 180° pulse (with the faster spins now chasing the slower spins) they return in a time $\tau$ to their original position. This forms an echo in the x'-y' plane (at time $t=2\tau$ following the 90° pulse) in part G of fig.(9). Hahn found that the application of the second pulse produced the echo, which he named "spin echo."

By recalling the concepts of relaxation, we see that as $\tau$ is lengthened, the spins have more time to dephase and return to thermal equilibrium along $H_o$. Therefore, the echo amplitude will diminish for increasing values of $\tau$ . By varying $\tau$ and applying different types of pulse sequences at resonance, (e.g. 90°-90° and 90°-180° pulses) we plot the recovery and spin-dephase functions, $1-\exp(-t/T_1)$ and $\exp(-t/T_2^*)$ respectively, and determine $T_1$ and $T_2^*$ [13] [17].

THE BLOCH EQUATIONS:

The equations of motion of the nuclear magnetization vector were first developed by F. Bloch [18] in a phenomenological approach using the information presented thus far. Later, the Bloch equations were rigorously deduced from first principles [19] given certain experimental constraints.

In order to give a thorough treatment of NMR, and hence

(a)

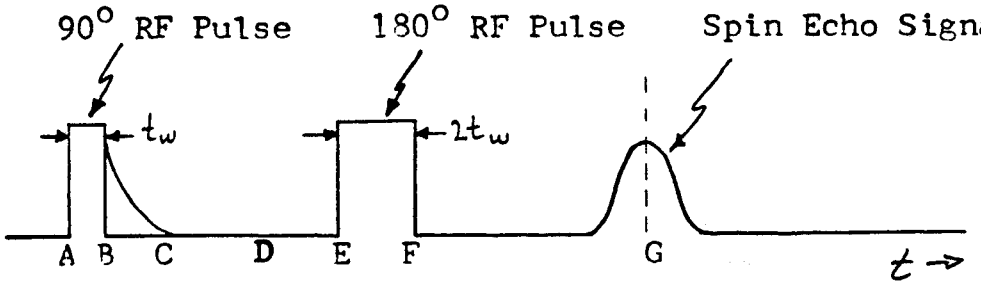


(b)

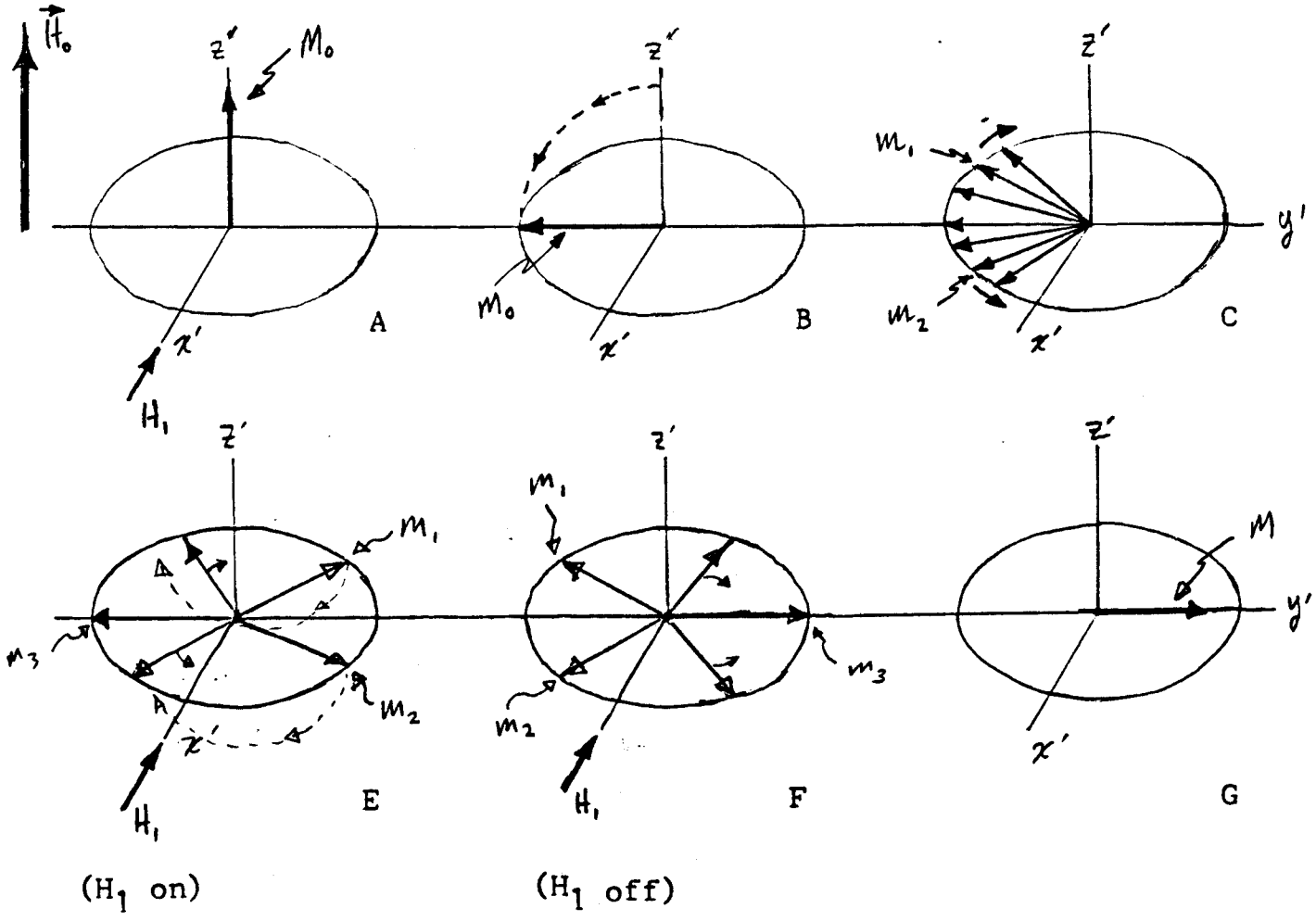


Fig. 9. (a) Spin Echo and pulse sequence in the time domain. (b) 90° pulse at A. Fanout at C. The 180° pulse is applied from E to F where the plane of isochromats of flipped. Constructive interference at G where the echo is formed ; $\vec{M}$ has deminished in amplitude from relaxation.

imaging, we solve the Bloch equations, since the behavior of $\vec{M}$ in a local volume of tissue ultimately provides the information about the spin density there.

The Bloch equations are reproduced here and solved for the time dependence of the free induction decay following the pulse field $H_1$. Most references provide the steady state solution for cw-NMR: $H_1$ continuously applied. We are interested in the behavior of $\vec{M}$ following the turn-off of $H_1$.

We seek a differential equation describing the motion of $\vec{M}$ under the influence of the total magnetic field $\vec{H} = \vec{H}_0 + \vec{H}_1$. The vector differential equation for the motion of a single moment is written classically for $\vec{\mu} = \gamma \vec{J}$

$$\frac{d\mu}{dt} = \gamma \vec{\mu} \times \vec{H} , \qquad (2)$$

which when summed over all moments of the population difference n in a unit volume of the sample contributing to $\vec{M}$, yields

$$\frac{dM}{dt} = \gamma \vec{M} \times \vec{H} . \qquad (3)$$

This equation, however, is incomplete; as we have seen, other effects contribute to $d\vec{M}/dt$, namely the processes of spin-lattice and spin-spin relaxation. Therefore, the longitudinal magnetization ($\vec{M}_z$) will grow while the transverse magnetization ($\vec{M}_x + \vec{M}_y$) decays, each exponentially with respective time constants $T_1$ and $T_2$.

In this way, the rate of change of $M_z$ due solely to spin-lattice relaxation effects is [18]

$$\frac{dM_z}{dt} = \frac{1}{T_1}(M_0 - M_z) , \qquad (4)$$

with the steady state solution $M_z = M_0 =$ constant. Combining eq.(3) for the z-component with eq.(4), we have for the first of Bloch's equations

$$\frac{dM_z}{dt} = \gamma(\vec{M} \times \vec{H})_z + \frac{1}{T_1}(M_0 - M_z) . \qquad (5)$$

Due to the distribution of local field values ($H_{loc}$) across the sample, the relative phase coherence among the nuclei is destroyed in a time $T_2^* \sim 1/\gamma H_{loc}$. Comparing this expression with the components $\dot{M}_{x,y} = \gamma(\vec{M}_{x,y} \times \vec{H})$, one obtains the contributions to the transverse magnetization

$$\frac{dM_x}{dt} = -\frac{M_x}{T_2^*} ,$$

and

$$\frac{dM_y}{dt} = -\frac{M_y}{T_2^*} . \qquad (6)$$

Integration of eqs.(6) immediately shows that these components decay exponentially with time constant $T_2^*$ following the resonant pulse, as expected.

Finally, by combining eqs.(3), (5), and (6), we obtain Bloch's phenomenological equations:

$$\frac{dM_x}{dt} = \gamma(M \times H)_x - \frac{M_x}{T_2^*} \quad ,$$

$$\frac{dM_y}{dt} = \gamma(M \times H)_y - \frac{M_y}{T_2^*} \quad , \qquad (7)$$

and

$$\frac{dM_z}{dt} = \gamma(M \times H)_z + \frac{M_o - M_z}{T_1} \quad .$$

The solutions to Bloch's equations of interest are those describing the motion of $\vec{M}$ as it returns parallel to $H_o$. The solutions to eq.(7) for the laboratory frame (Append. B) are

$$M_x = M_{T_o} e^{-t/T_2^*} \cos\omega_o t \quad , \qquad (8)$$

$$M_y = -M_{T_o} e^{-t/T_2^*} \sin\omega_o t \quad , \qquad (9)$$

and

$$M_z = M_o (1 - e^{-t/T_1}) \quad . \qquad (10)$$

$M_{T_o}$ is the amplitude of the components of transverse magnetization.

These equations are as we expected and give $\vec{M}$ $(M_x, M_y, M_z)$ in the laboratory frame. Note that the transverse magnetization $\vec{M}_T$ $(=\vec{M}_x + \vec{M}_y)$ decays with time constant $T_2^*$ in fig.(10) and equals $M_o$ at t=0.

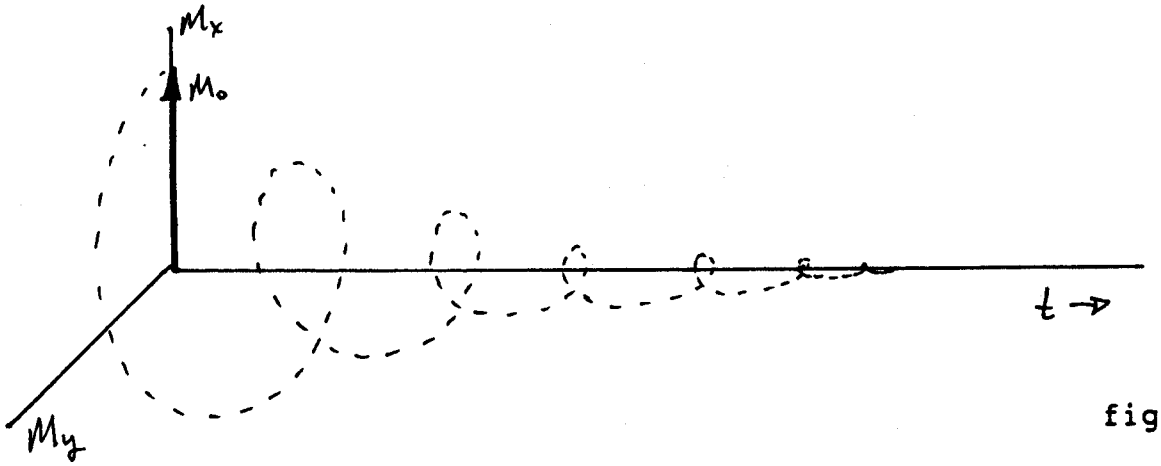


fig.(10)

At $t=\infty$, $M_T = 0$ and $M_z = M_o$ when thermal equilibrium has established itself within the sample from relaxation effects. In a frame rotating at $\omega_o$, the Bloch equations reduce to (Append. B)

$$M_{x'} = M_{ox'} e^{-t/T_2^*} , \qquad (11)$$

$$M_{y'} = M_{oy'} e^{-t/T_2^*} , \qquad (12)$$

and

$$M_{z'} = M_{oz'} \left(1 - e^{-t/T_1}\right) . \qquad (13)$$

which show the respective decays and growths without rotations. $M_{ox'}$ and $M_{oy'}$ are the initial magnitudes of $M_{x'}$ and $M_{y'}$; $M_{z'} = M_z$, and $M_{oz'}$ is the equilibrium value of $M_z$.

An FID contains all the information about a sample. In spectroscopy, the response of resonant nuclei are superposed within the FID signal, whereas in imaging, information about spin density $\rho(\vec{r})$ of $^1H$ nuclei and their location are superposed in the FID.

In the next section, we consider the application of pulse-NMR imaging presently being used in medicine. It is a young field in rapid growth.

## VI. Pulse Nuclear Magnetic Resonance Imaging

Recall that the $^1H$ nucleus, distributed in different concentrations throughout the body in water and lipids, is detected by the imager. Practically all other nuclei go undetected since their Larmor precessions are not near the frequences within the bandwidth of the rf pulse.

Pulse-NMR imaging, often called magnetic resonance imaging (MRI), is almost exclusively used in diagnostic medicine. As we will see, MRI techniques produce images from the information contained in the FID following the $90^\circ$ pulse. A major advantage to MRI is that it safely views the contents of living tissue, unlike X-ray computed tomographic (CT) scans with their damaging X-radiation.

An MRI apparatus may locate a point, line, plane or volume within the sample. In this paper, we show how images are produced by plane selection. Planar imaging can be performed several ways; however, all methods use linear field gradients $\vec{G}$ (Gauss/cm) in addition to $H_o$. The field $\vec{G}$ selects a plane from which to image, and spatially encodes coordinate information within that plane.

There are various scanning techniques that provide different kinds of information. We shall consider only two methods: (1) The Projection Reconstruction Algorithm and (2) Two-Dimensional

Fourier Zeugmatography using Spin-Echo Pulse Sequence. The first of the above techniques is historical whereas the second is one currently used in medicine.

(1) Projection Reconstruction Algorithms:

The first published NMR image was created by Paul C. Lauterbur [20] of the State University of New York at Stony Brook, where in 1973 he produced images of two water-filled capillary tubes. He called his technique Zeugmatography (from the Greek zeugma, which means "to join," signifying the coupling between the rf and gradient fields).

The application of a linear magnetic field gradient $\vec{G}$, in addition to $H_o$, across the sample produces a linear distribution of Larmor frequencies in the direction of $\vec{G}$. The FID signal following an rf pulse is an interference pattern of frequencies that is a function of position in the direction of $\vec{G}$. The sample spin density $\rho(\vec{r})$, the effective spin density distribution at the point $\vec{r}$, varies according to position, causing the signal's amplitude to change in intensity proportionally to $\rho(\vec{r})$. Upon Fourier transformation of the FID, spatial and intensity information is displayed in the frequency domain.

In fig.(11-a) [21], the FID following the rf pulse is a decaying monochromatic source, which shows the single emission frequency after Fourier transformation. By applying the linear

field gradient $\vec{G}$ in fig.(11-b), each adjacent strip of water molecules precess at successively higher frequencies in the direction of $\vec{G}$. A stronger emission signal is observed at frequency $\nu'$ since more $H_2O$ molecules precess at that frequency than those preceding it.

P. Mansfield and P. G. Morris have shown that the envelope of the complex normalized FID signal in fig.(11-b) may be written [22]

$$S(t) = \int \rho(\vec{r}) \exp\left[i\gamma \vec{r} \cdot \int_0^t \vec{G}(t')dt'\right] d\vec{r} \,, \qquad (1)$$

where G(t) is the general field gradient of the magnetic flux density ($\vec{G}=\nabla H_z$) and t is the time after the 90° pulse. For times $t \simeq T$, the right side of eq.(1) should be multiplied by $\exp(-t/T_2)$.

Fig.(11-c) [21] shows Lauterbur's method where $\vec{G}$ is applied in different directions. Equivalently, the sample may be moved with respect to $\vec{H}_o$ and $\vec{G}$. Finally, Lauterbur reconstructed the sample image by using a projection-reconstruction algorithm (e.g. [23] [24]) which uses a computer to reconstruct images from a minimum number (2 or 3) of projections.

(2) Two-Dimensional Fourier Zeugmatography:

This technique has similarities with the previous technique;

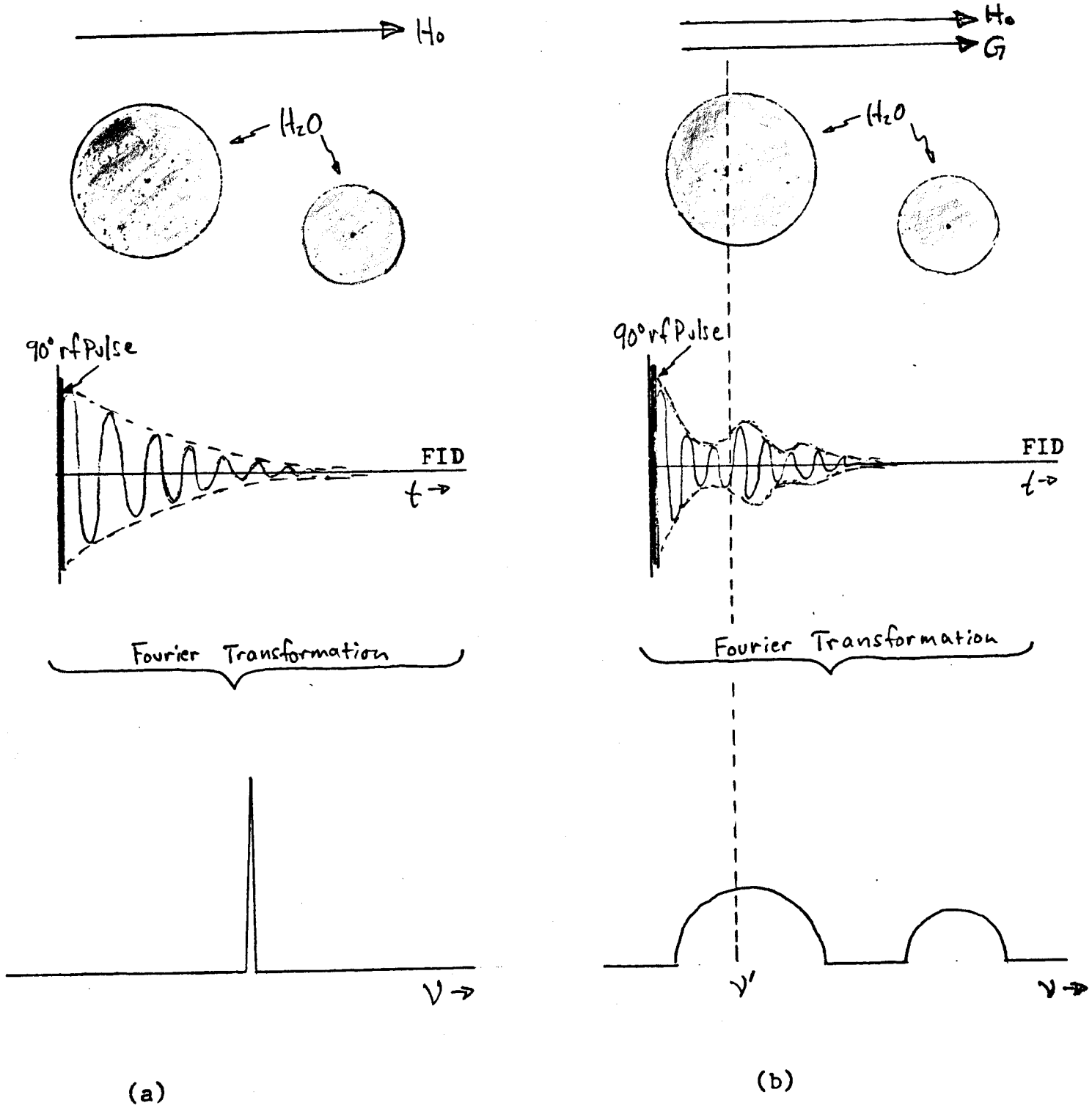


Fig. 11 a-b. Fourier transform of the FID, (a) without gradient, (b) with gradient. Note the spatial reconstruction in the frequency domain of (b).

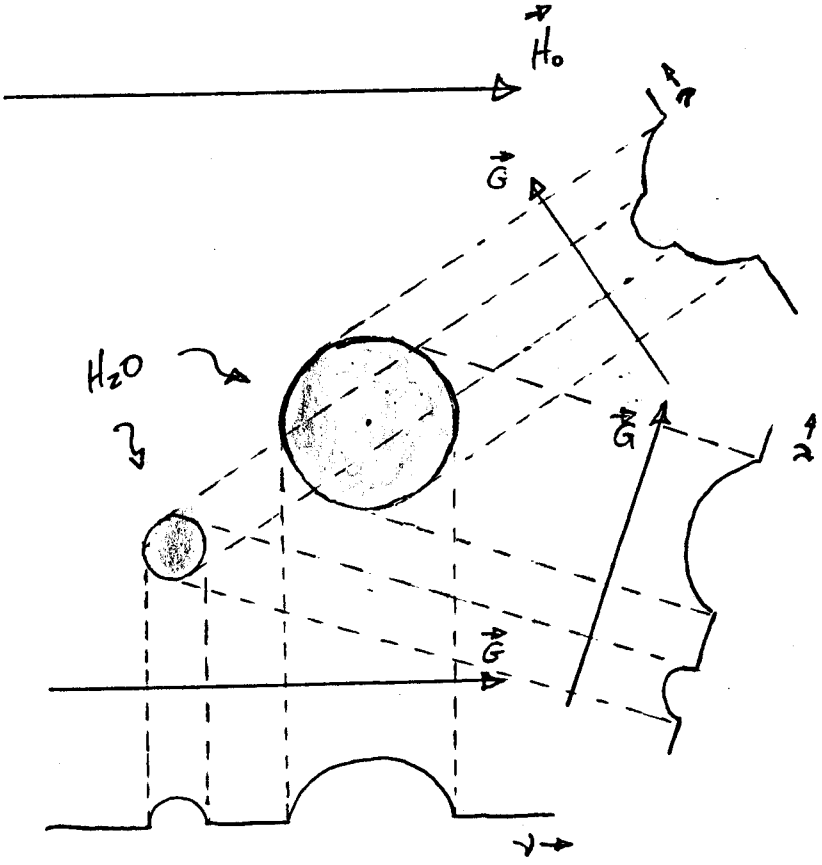


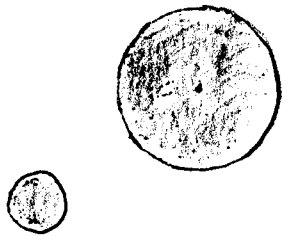

Reconstructed image

Fig. 11-C. Projection-reconstruction imaging. The magnetic field gradient is rotated through at least 180° to obtain projections of the image (top view of $H_2O$-filled capillary tubes here). With the data of some minimum number (two or three) of projections, a computer reconstructs the cross-sectional image of the sample.

the main differences are that additional gradients are used instead of one, a second Fourier transform is used following the first, and no algorithm is used here. Before we continue, we will explore some details of the gradient and rf pulse fields.

## THE MAGNETIC FIELD GRADIENT:

The magnetic field gradient $\vec{G}$ is applied across the sample in directions that are independent of the direction of $\vec{H}_o$. As $\vec{G}$ creates a linear distribution of Larmor frequencies, each position is converted to a frequency change $\Delta\omega_z$, which $\omega_o = \gamma H_o$ gives as $\Delta\omega_z = \gamma G_z \Delta z$. The total field gradient $\vec{G}$ is described by a tensor of the second order [5]. However, for static field strength $H_o \hat{k} \gg |\vec{G}|$, we neglect terms involving changes in the transverse magnetic flux density. Therefore,

$$\vec{G} = \nabla H_z = (\nabla \vec{H}) \cdot \hat{k} . \qquad (2)$$

As we shall see, the linear magnetic field gradients $G_z = \partial H_z / \partial z$, $G_x = \partial H_z / \partial x$, and $G_y = \partial H_z / \partial y$ are applied as "pulses" in intervals particular to the experiment involved. The mutual orthogonality of the gradients provides selection of a plane and distance encoding within that plane. The effect of gradient switching will make sense after we consider the Fourier transform of the rf pulse.

PULSE DYNAMICS AND THE FOURIER TRANSFORM:

Central to magnetic resonance imaging are some basic Fourier transform theorems, and the frequency response of the rf pulse on the magnetization, (see [25], ch.3).

What, precisely, is the frequency distribution of an rf pulse? In order to form a pulse with finite length $t_w$ (time domain), its carrier is modulated such that the rising and tailing edges are formed via its Fourier series. The pulse width $t_w$, then, produces a distribution of frequencies that goes as $1/t_w$. For example, a pulse of $t_w = 2\mu s$ has a bandwidth of 500 KHz, which will resonate all nuclei in the sample whose Larmor frequency lies within +/-250 KHz of the carrier.

To be more precise, the frequency distribution of an rf pulse can be obtained by considering the transformation equations [25]

$$F(\omega) = \int_{-\infty}^{\infty} f(t)\exp(^{+}i\omega t)dt \equiv \mathcal{F}^{+}f(t) , \qquad (3)$$

$$f(t) = \frac{1}{2\pi}\int_{-\infty}^{\infty} F(\omega)\exp(-i\omega t)d\omega \equiv \mathcal{F}^{-}F(\omega), \qquad (4)$$

where $\mathcal{F}^{+}$ and $\mathcal{F}^{-}$ are the Fourier inverse and transform respectively. Since our pulse function $f(t)$ is even and exists only for t>0 (the limitation called causality) we can simplify eq.(4)

using the cosine transform since it is real and even in the time domain (this shall not be proved here, see [25]). Therefore, by taking the pulse's lower limit at $t=-t_w/2$, so that $t=0$ is centered on the pulse, we have for the frequency spectrum

$$F(\nu) = \frac{1}{t_w}\int_{-t_w/2}^{t_w/2} \cos 2\pi\nu t \, dt = \frac{\sin \pi\nu t_w}{\pi\nu t_w}, \quad (5)$$

which is defined as the sinc function. It looks like a damped cosine function for 1/x, except with height $1/t_w$ at the carrier where x=0, see fig.(12).

PLANE SELECTION:

Planar imaging requires two steps: First, nuclei in a given slice $\Delta z$ are excited. Second, spatial information is encoded along x and y, see fig.(13). The slope of the gradient (Gauss/cm) and the rf pulse width determine slice thickness. For example, a sample of $^1H$ nuclei ($\gamma = 2.68 \times 10^4$ rad/sG) in a gradient of 0.3 G/cm produces a variation of 1.28 KHz across one cm of sample in the direction of the gradient. And, the bandwidth of a 1.0 ms pulse is 1.0 KHz. Therefore, the slice thickness in a sample with this, roughly typical, pulse and gradient is 0.8 cm and forms a plane perpendicular to $\vec{G}$. For enhanced resolution, the slice thickness is made much smaller: typically one millimeter. Finally, the location of the slice is easily changed by applying a dc offset to the slice-selection gradient and/or by

moving the rf carrier.

SPATIAL ENCODING:

Next, we need to spatially encode distance information along the axes of the plane slice. This is done by first applying the slice-selection gradient $G_z$ for the same duration as the rf pulse, which flips the spins into the x-y plane, see fig.(14) [21] [26]. When $G_z$ is turned off, the second gradient, $G_y$, is turned on orthogonal to $G_z$ for a short time $t_y$ making phase a function of position along the y-axis of the slice. Following the shut-off of $G_y$, both the receiver and final gradient $G_x$ is turned on. $G_x$ is applied perpendicularly to the previous two. The FID is then obtained and Fourier-transformed. This process is typically repeated for some 120 values of the phase encoding gradient $G_y$ increasing in magnitude from zero. Figure (15) illustrates the train of gradients. Each phase-encoded projection is stacked in the order in which the $G_y$'s were applied. Then, the corresponding points from each projection are Fourier transformed to generate the final image. Fast Fourier Transform (FFT) computers are used to make each of the required Fourier transforms.

For biological samples with $T_1$'s of 0.1 to 2-3 s, a recycle time $t_r$ is needed between data acquisition to allow the spins to return to equilibrium with $H_o$; $t_r=3T_1$ in general [26].

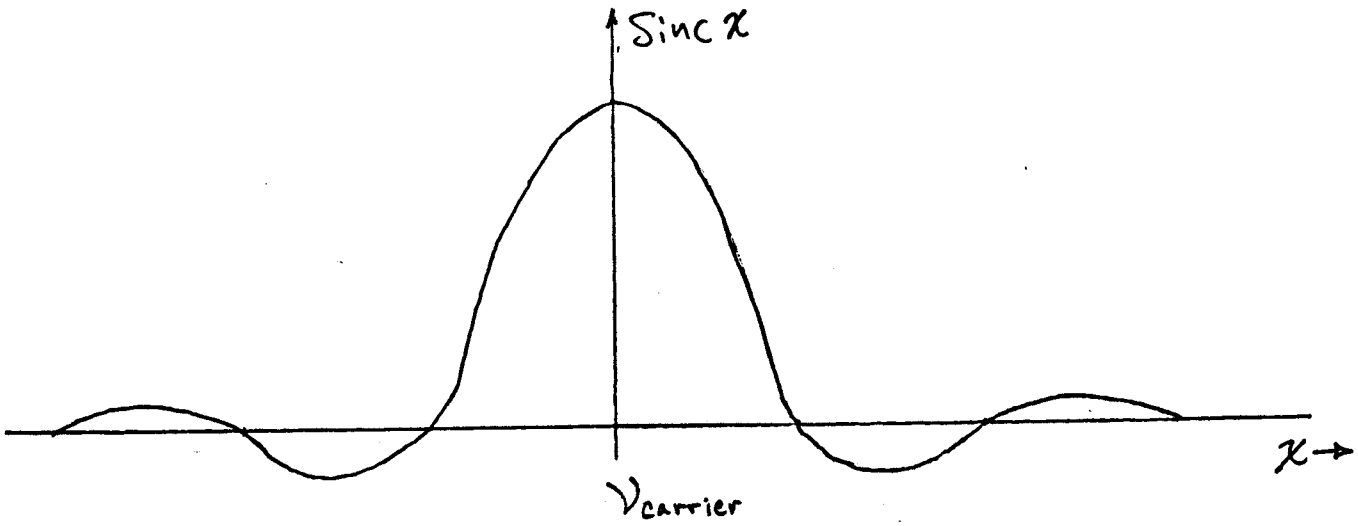


Fig. 12. The frequency response of a square pulse with finite length is the sinc function. By definition, $\text{sinc}(x)=\sin \pi x/\pi x$.

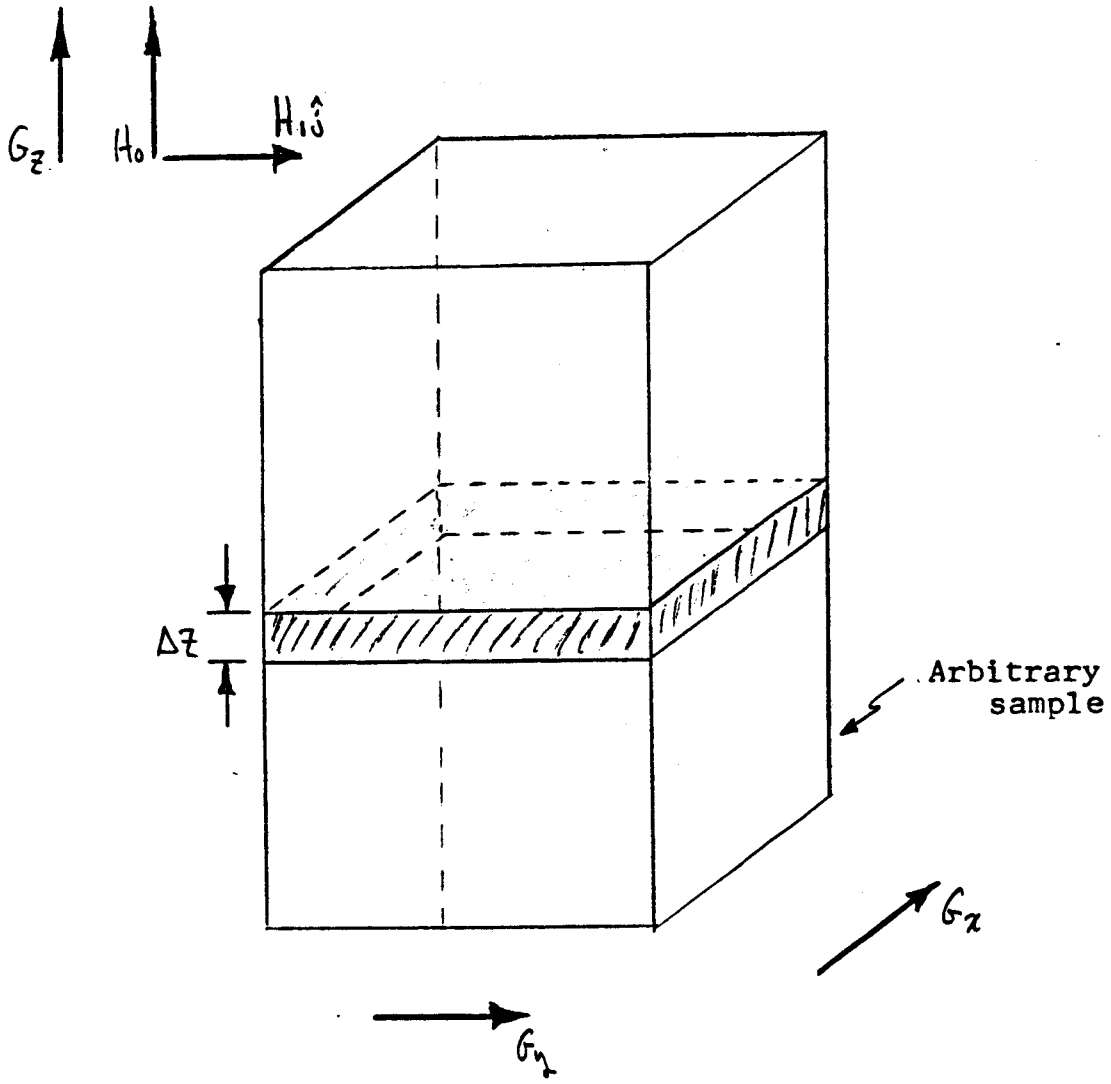


Fig. 13. Plane selection in a sample is done using the gradient $G_z$ and pulse fields $H_1$. The gradients $G_x$ and $G_y$ are used for spatial encoding along x and y.

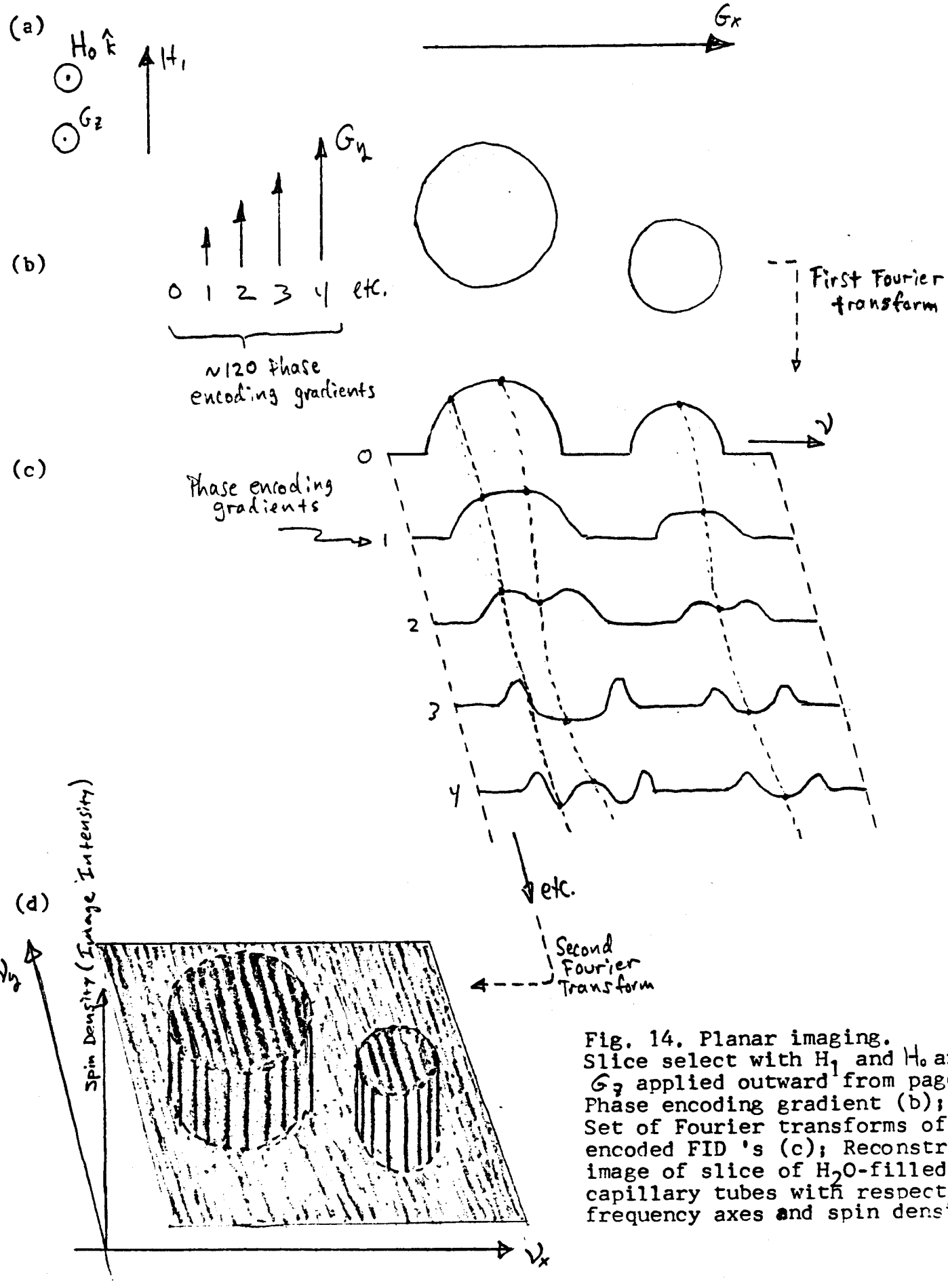


Fig. 14. Planar imaging. Slice select with $H_1$ and $H_0$ and $G_z$ applied outward from page (a); Phase encoding gradient (b); Set of Fourier transforms of phase encoded FID 's (c); Reconstructed image of slice of $H_2O$-filled capillary tubes with respective frequency axes and spin density (d).

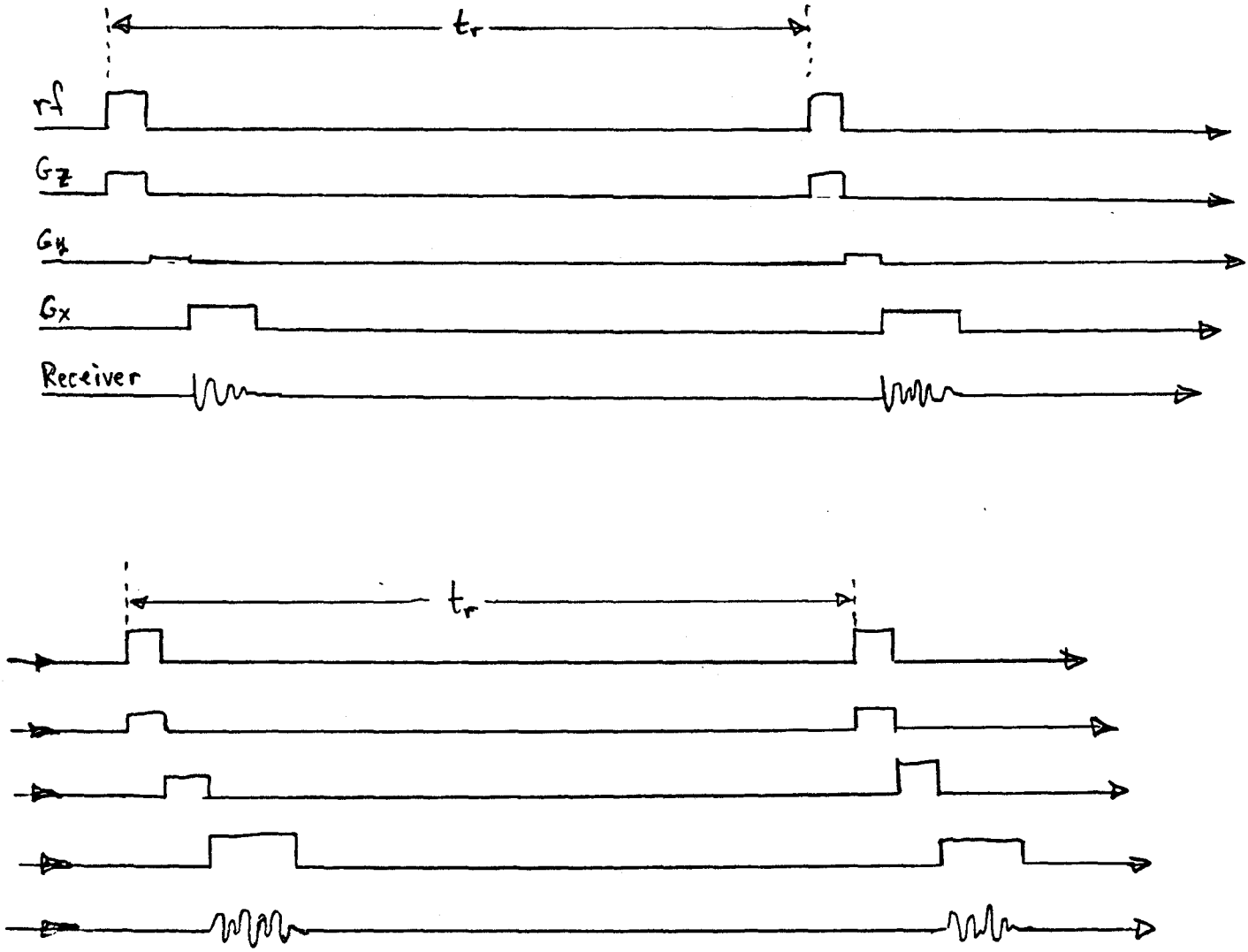


Fig. 15. Gradient train typical of planar imaging techniques. Note the increase in amplitude of the phase encoding gradient $G_y$ at each pulse. Also note the relaxation time $t_r$ between each pulse.

Therefore, it takes about 2-10 min to produce a single-slice image.

At this point, some details need to be filled in. After obtaining the FID's (which possess all the amplitude (spin density) and spatial information about the sample) they are digitally stored. Typically, 512 bits of data are required for each FID. Following Fourier transformation, a "graph" of the data is created in the frequency domain with the sample coordinates and spin density arranged on three orthogonal frequency axes (as in fig.(14-d)).

In order to create a digitized image, the data is converted to a graph of typically 256 X 256 picture elements or pixels. For each pixel two pieces of information are required: an address, as for a matrix element, and an intensity of typically 15 gray-tones. Finally, an image is created with the stored data, where spin density is reproduced as pixel intensity and the location of $^1H$ nuclei are addressed to the proper pixel.

PULSE SEQUENCES:

What remains in the process of producing images is a means of manipulating the sample to enhance areas of interest and suppress areas of unimportance.

Variations in the values of $T_1$ or $T_2$ for specific biological

tissues are used to manipulate image contrast between different regions within the sample. Certain pulse sequences are used to emphasize either $T_1$ or $T_2$ values. Several pulse sequences can produce images; however, we will examine the saturation-recovery sequence and the spin-echo pulse sequence, the latter used to produce the images appearing in this paper.

In the saturation-recovery sequence, a train of 90° pulses is applied with interpulse spacing $\tau$, where $\tau \sim T_1 > T_2$ for $^1H$ nuclei (see fig.(16)). If the complete spin-spin relaxation process occurs during $\tau$, the amplitude of the FID will be dependent on $T_1$ and the concentration of $^1H$ nuclei contributing to the signal. Nuclei whose $T_1$ values are long compared to $\tau$ will yield weak signals. By changing the value of $\tau$, variations in $T_1$ at different locations in the sample will yield differences in image intensity. By combining two or more images with different values of $\tau$ it is possible to assign a $T_1$ value for each pixel. The resultant image becomes a "$T_1$-map."

Another sequence, called the Carr-Purcell sequence [17], incorporates the spin-echo. In this sequence, images are dependent on the spin-spin relaxation time $T_2$. A sequence of spin-echos is produced by applying an initial 90° pulse followed by a series of 180° pulses spaced by $(2n+1)\tau$ with n=0,1,2,... (see fig.(17)).

Recall that $T_2^*$ relaxation effects are a combination of natural $T_2$ effects and inhomogeneities in $H_o$, and that fanout is determined by $T_2^*$. The 180° pulse has the effect of reversing the

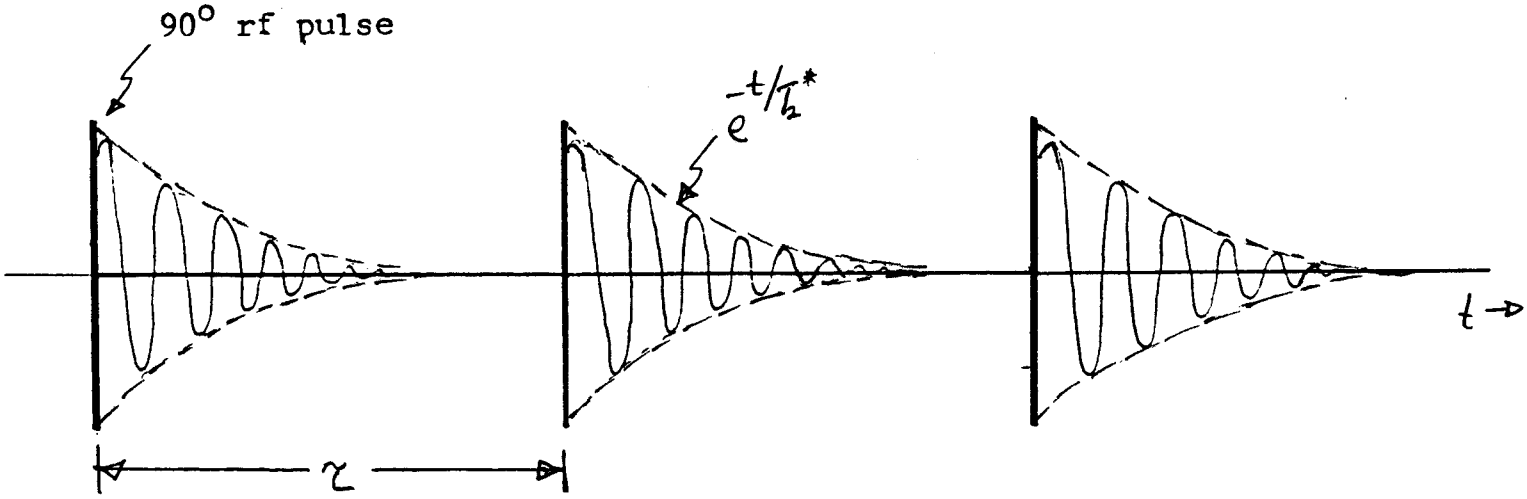


Fig. 16. Saturation-Recovery Sequence. A train of 90° pulses is applied with interpulse spacing $\tau$ where $T_2 < \tau \sim T_1$. Images obtained using this method are $T_1$-weighted since $T_2^*$ interactions loose complete phase coherence during the time $\tau$.

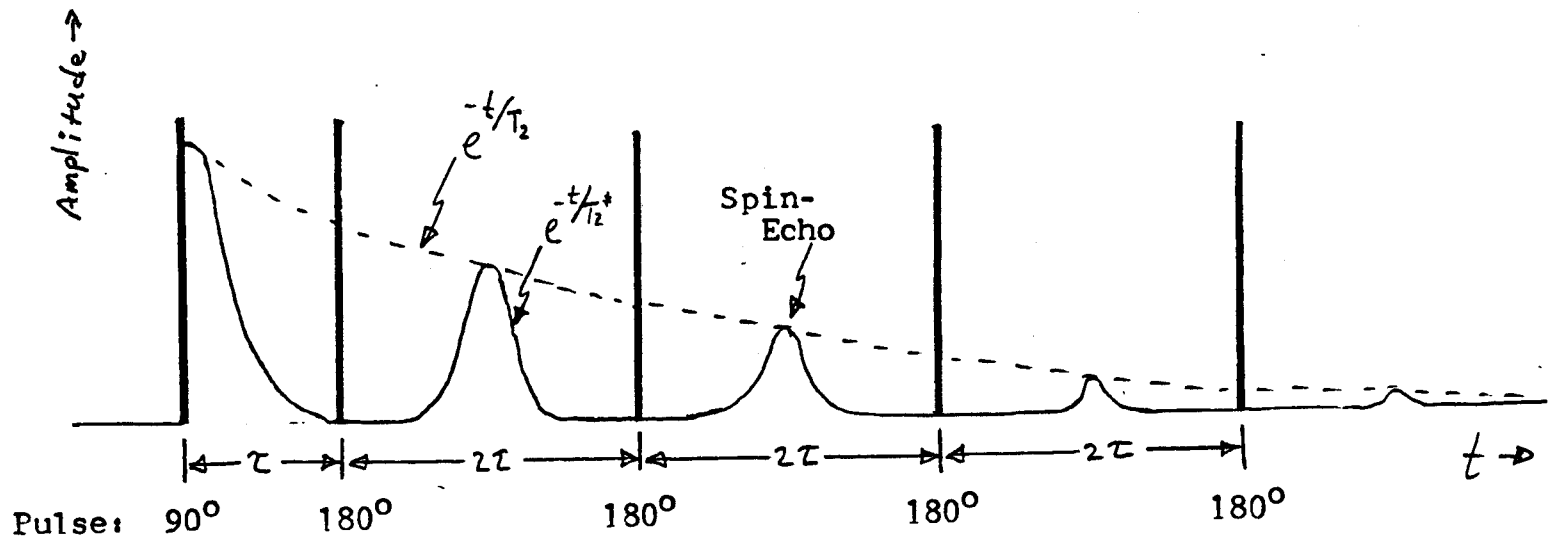


Fig. 17. Spin-Echo Pulse Sequence. Images obtained using this method are $T_2$-weighted since $\tau \sim T_2 < T_1$ and since the echo amplitude decays via $T_2$-effects only.

isochromats such that the decay in echo maxima, at $2(n+1)\tau$ after the 90° pulse, corresponds to natural $T_2$ effects only and field inhomogeneities are ignored. Hahn in fact developed the echo technique for this purpose.

Acquisition of the echo train (when the receiver is on) occurs on the second half of each echo. The decay tail of each echo is an FID identical to that following the 90° pulse except for the amplitude decrease due to $T_2$-relaxation, which occurs during the interval $2\tau$.

If the $T_2$'s of different nuclei within the sample are sufficiently different and $\tau$ is chosen such that the magnetization in the x'-y' plane from shorter $T_2$'s have relaxed to zero at time $2\tau$, only those nuclei with $T_2$'s longer than $\tau$ will be observed after Fourier transformation of the second half of an echo [27]. In this way, the choice of $\tau$ provides the mechanism for image manipulation, and the images are said to be $T_2$-weighted.

Some imagers apply a Carr-Purcell sequence to collect data from several echos following a single spatial encoding sequence. For example, four images can be produced from four echos within a single slice in order to reduce imaging time and enhance S/N.

The spin-echo pulse sequence is an especially good image sequence for locating tumors, besides being a good image technique. The differences between $T_2$ values of cancerous tissue and corresponding normal tissue creates a contrast in the image at a tumor location; $T_2$ for tumors are long compared to $T_2$ of normal

tissue.

Refer again to figs.(A-C) with the concepts of imaging in mind. The explanation of important terms, in caption, should now be clear.

INSTRUMENTATION:

Whole-body imagers use large magnets with a 1 m free bore where a human (or other subject of similar size) is placed. They use electromagnets with field strengths of 0.15 to 0.3 Tesla ($1T = 10^4 G$) detecting proton resonance at 6MHz to 12MHz. Superconducting solenoids of 0.5T to 1.0T (21MHz to 42.5MHz) are common. The images of figs.(A-C) were created with a high-field superconducting electromagnet at 1.5T (64MHz). A high field strength is desired because sensitivity is greater. The homogeneity in the static field of modern imagers is on the order of 0.1 ppm across roughly 15cm.

Fig.(18) (adapted from [21]) shows a subject in an imager. The four large coils generate the static field $H_o$. The rf field is generated by a coil in the form of two curved panels and is used to receive the NMR signal induced by the rf field. The NMR signal is then sent to a computer where the images are processed.

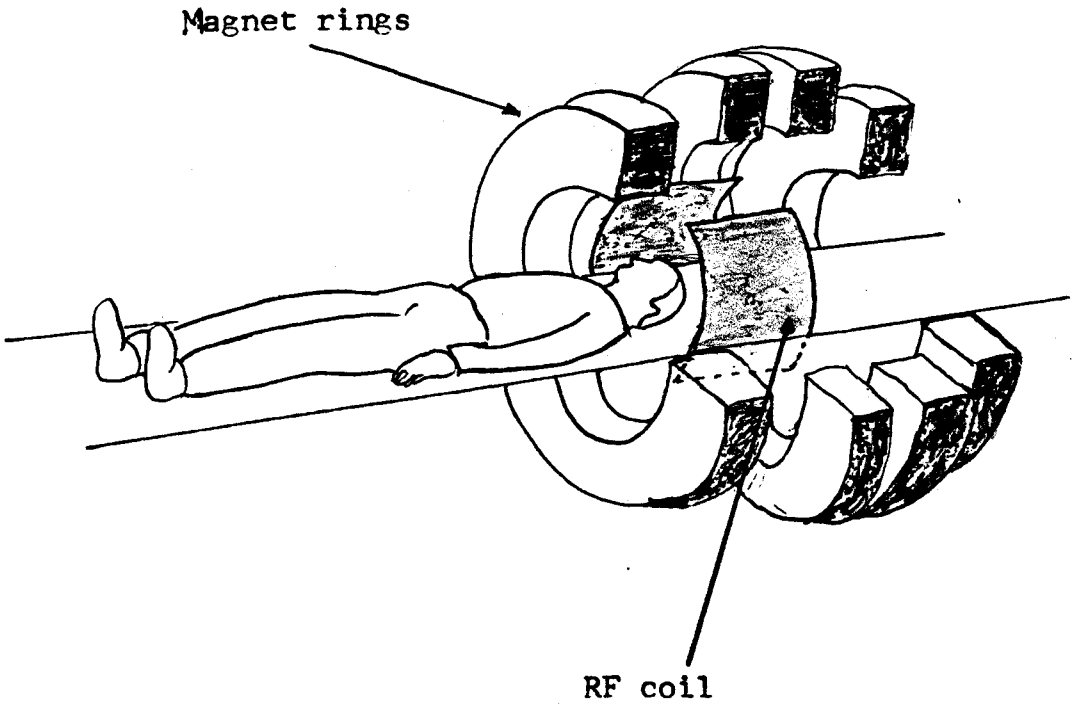


Fig. 18. Whole body imaging apparatus. The four large rings have coils that generate the static field $H_o$. The two curved panels generate the radio-frequency pulse and receive the emitted NMR signal.

## VII. Conclusion

NMR imaging is still at an early development stage. Much data must be accumulated so that more efficient techniques can be developed.

In the first four sections of the paper, we discussed many details of NMR (with highlights on imaging): physical principles of the nucleus, the quantum mechanical description of an isolated spin in a static magnetic field, the magnetic effects of a sample at thermal equilibrium in the static field, and a detailed theory of resonance including the classical Bloch equations describing the behavior of the magnetization vector $\vec{M}$ following an rf pulse.

In the final section, we described two imaging techniques. First, we presented the original imaging method: produced by Paul C. Lauterbur in 1973 using projection reconstruction algorithms to construct an image from projections made by gradient fields and Fourier transformation of the NMR signal induced by a radio-frequency pulse. Second, we described the technique of imaging to create the images of figs.(A-C), called Fourier Zeugmatography, where a Fourier transform is used twice to spatially decode distance information put into the sample by gradient fields. We then gave a few details of the signal image processing method employed by all imagers. Finally, a sub-section on instrumentation was added where the apparatus of whole-body imaging is discussed.

This new field of imaging (Fourier Zeugmatography), using the physics of NMR, has a great potential in diagnostic medicine. Unlike ct-scans, an imaging system that uses hazardous X-rays, magnetic resonance imaging uses only magnetic fields which are harmless biologically. Also, magnetic resonance imaging can locate tumorous tissues very accurately; they show up as bright spots on the negative image. Although magnetic resonance imaging is a new technology, with many areas of potential improvement, it is, in fact, proving itself today as an extremely useful tool.

## ACKNOWLEDGEMENTS

(1) Much thanks go to Frank Bridges, my technical advisor, for his technical support.

(2) I wish to thank John Rider, technician at the MRI center at Dominican Hospital in Santa Cruz, for his generosity in providing the echo-planar images which appear in this paper.

## REFERENCES


(1) Images from General Electric Company's 1.5T Signa system operating at the Dominican MRI center in Santa Cruz, CA, created in December, 1985.

(2) Purcell, Torrey, and Pound, "Physical Review." 69, 37 (1946).

(3) Bloch, Hansen, and Packard, "Physical Review." 69, 127 (1946).

(4) Fukushima, E., and S.B.W. Roeder. Experimental Pulse NMR, a nuts and Bolts Approach. Don Mills: Addison-Wesley, 1981.

(5) P. Mansfield, and I.L. Pykett, "J. Mag. Res." 29, 355 (1978).

(6) Kramer, D.M. NMR Imaging in Medicine. New York: Igaku-Shoin,1981.

(7) Feynman, R. P., R. B. Leighton, and Matthew Sands. The Feynman Lectures on Physics, Vol. II. Menlo Park: Addison-Weslwy, 1963.

(8) Winter, Rolf G. Quantum Physics. Belmont: Wadsworth Publishing Co., 1979.

(9) G.E. Pake, "Solid State Physics." 2, 1 (1956).

(10) Slichter, Charles P. Principles of Magnetic Resonance. New York: Harper & Row, 1963.

(11) Park, David. Introduction to the Quantum Theory. New York: McGraw-Hill, Inc., 1974.

(12) Schumacher, Robert T. Introduction to Magnetic Resonance. New York: W. A. Benjamin, Inc., 1970.

(13) E.L. Hahn, "Physical Review." 80, 580 (1950).

(14) Poole, Charles P., and Horacio A Farrach. Relaxation in Magnetic Resonance. New York: Academic Press, Inc., 1971.

(15) Abragam, A. The Principles of Nuclear Magnetism. New York: Oxford University Press, 1961.

(16) E.L. Hahn, "Physics Today." 6, 4 (1953).

(17) Carr, and Purcell, "Physical Review." 94, 630 (1954).

(18) F. Bloch, "Physical Review." 70, 460 (1946).

(19) R.K. Wangsness and F. Bloch, "Physical Review." 89, 728 (1953).

(20) P.C. Lauterbur, "Nature." 242, 190 (Mar. 1973).

(21) I.L. Pykett, "Scientific American." 246, 78 (May 1982).

(22) P. Mansfield and P.G. Morris, Suppl. 2, "Advances in Magnetic Resonance, the Principles of Biological and Medical Imaging by NMR," Academic Press, New York, 1982.

(23) R.N. Bracewell, and A.C. Riddle, "Astrophysical J." 150, 427 (1967).

(24) R. Gordon, and G.T. Herman, "Comm. Assoc. Comput. Mech." 14, 759 (1971).

(25) Shaw, Derek. Fourier Transform N.M.R. Spectroscopy. New York: Elsevier Scientific Publishing Co., 1976.

(26) S.L. Smith, "Anal. Chem." 57, 595A (Apr. 1985).

(27) D.L. Rabenstein, "Anal. Chem." 50, 1265A (Nov. 1978).

Figures (A-C): Created by General Electric's 1.5 Tesla Signa system imager. They are cross-sectional images of human tissue. The imaging technique is the multiple spin-echo pulse sequence described in the text. TE noted in each image is the interpulse spacing $\tau$ in ms; data acquisition time is shown in min., and each was created using 256 x 256 pixels. The fine detail is attributed to a large S/N and a uniform static field $H_o$. Dark regions correspond to a near zero spin density of $^1H$ nuclei. Light regions correspond to a high concentration of free water and/or lipids (fats and oils) which contain $^1H$ nuclei in large amounts. Bone, with close to zero $^1H$ nuclei, appears dark in the skull and vertebra.

Fig. A Cervical spine; areas of low signal intensity, as indicated by arrow, represent the spinal cord mass (an area of low $^1H$ concentration).

TE= $\tau$ =25ms

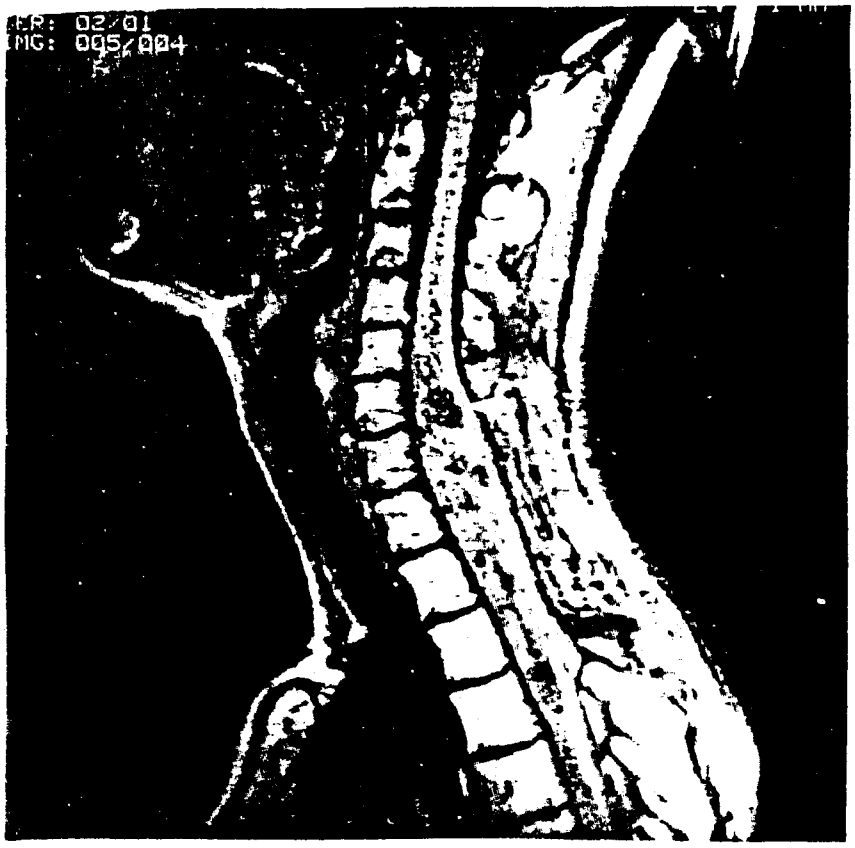

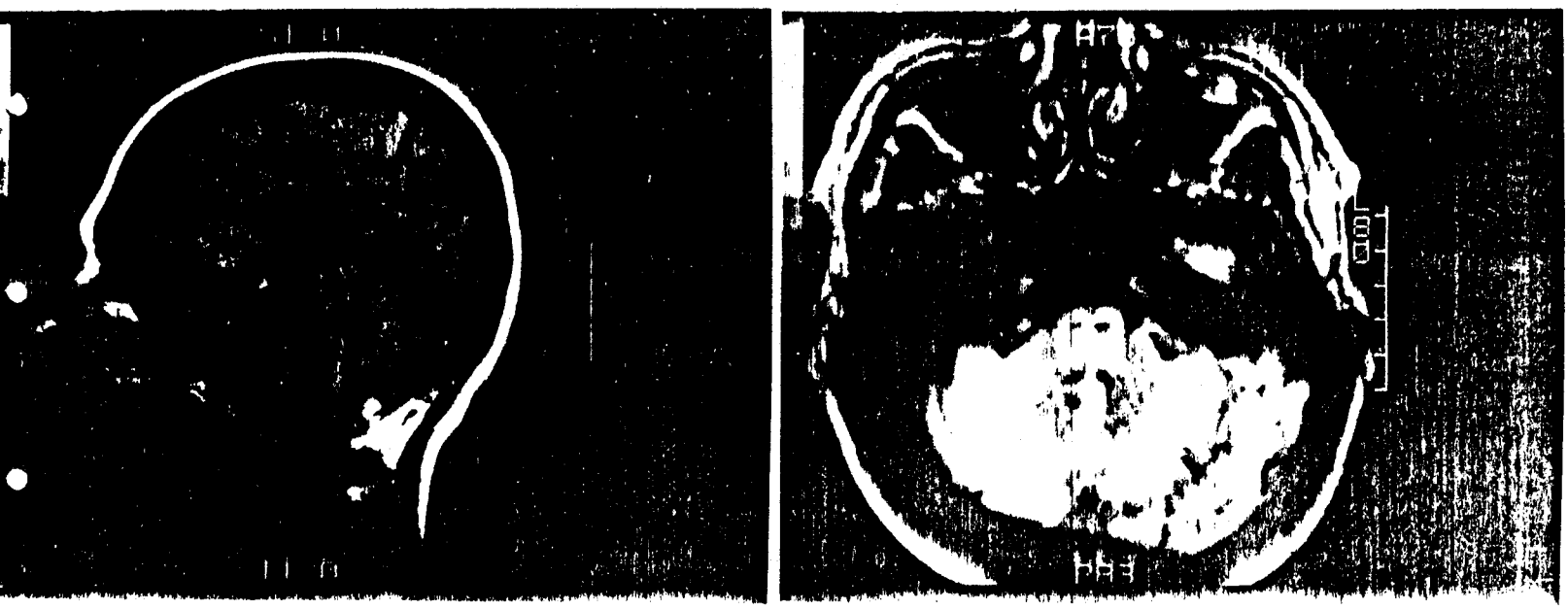

Fig. B

TE= $\tau$=25ms

5 mm thick images of head: side view at left, top view at right.

Fig. C 3 mm thick image of the pelvis of a female with pelvic cyst, indicated by arrow.

TE= $\tau$ = 25ms

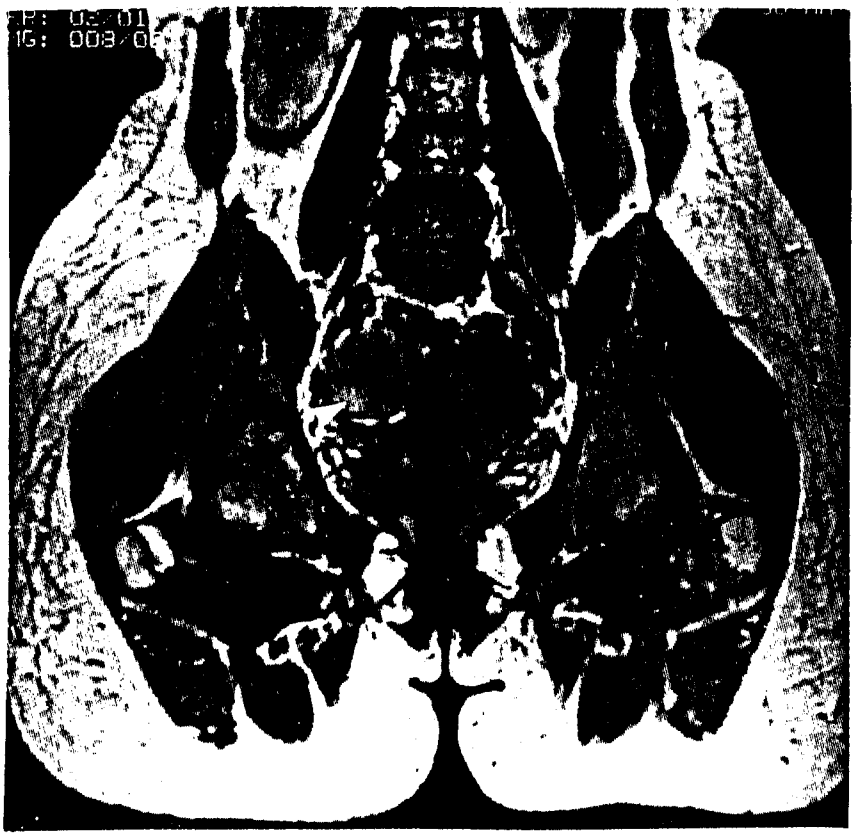

## XI. APPENDIX A

**Expectation values $\langle\hat{\mu}_x(t)\rangle$, $\langle\hat{\mu}_y(t)\rangle$ and $\langle\hat{\mu}_z\rangle$ for the magnetic moment $\hat{\mu}(t)$ of a spin in a static magnetic field:**

The expectation value of the magnetic moment $\hat{\mu}(t)$ is given by the expression

$$\langle\hat{\mu}(t)\rangle = \int_{-\infty}^{\infty} \Psi^* \hat{\mu}\, \Psi\, d\tau\,, \qquad \text{(a-1)}$$

where the term $\Psi$ is the state function containing all the information about the system and $d\tau$=dxdydz. Beginning with the x-component, we have

$$\langle\hat{\mu}_x(t)\rangle = \int_{-\infty}^{\infty} \Psi^* \hat{\mu}_x\, \Psi\, d\tau\,. \qquad \text{(a-2)}$$

In order to calculate this equation, we need only an expression for $\Psi$ and $\hat{\mu}_x(t)$.

Having found the energy eigenvalues in eq.(3) sec. III by considering how $\hat{\mu}$ interacts with $H_o$, we can express the corresponding time-dependent eigenfunctions $\psi_{j,m}$ of the Hamiltonian operator by using the separation of variables $\psi_{j,m}(\vec{r},t) = u_{j,m}(\vec{r})\,T(t)$. (The time-dependent phase factor is easily solvable [8]: $T(t)=e^{-iE_m t/\hbar}$.) And the particular form of $u_{j,m}$ may remain ambiguous for now, where

$$\psi_{j,m} = u_{j,m} e^{-iE_m t/\hbar} \qquad \text{(a-3)}$$

Utilizing the "completeness" of the eigenfunctions of the Hermitian Hamiltonian operator, the state function and its complex conjugate are

$$\Psi = \sum_m a_m \psi_{j,m} \quad ; \quad \Psi^* = \sum_n a_n^* \psi_{j,n}^* . \qquad \text{(a-4)}$$

We may now express the expectation value $\langle \hat{\mu}_x(t) \rangle$ by substituting eqs.(a-3),(a-4) and $\hat{\mu}_x = \gamma\hbar \hat{J}_x$ ( $\hat{J}_x$ dimensionless here) into eq.(a-2) in which case

$$\langle \hat{\mu}_x(t) \rangle = \int_{-\infty}^{\infty} \left(\sum_n a_n^* \psi_{j,n}\right) \gamma\hbar \hat{J}_x \left(\sum_m a_m \psi_{j,m}\right) d\tau$$

$$= \sum_{n,m} \gamma\hbar a_n^* a_m \left[e^{iE_n t/\hbar} e^{-iE_m t/\hbar}\right] \int_{-\infty}^{\infty} u_{j,n}^* J_x u_{j,m} \, d\tau$$

$$= \sum_{n,m} \gamma\hbar a_n^* a_m \langle n|\hat{J}_x|m\rangle e^{(i/\hbar)[E_n - E_m]t} \qquad \text{(a-5)}$$

In Dirac's 'bra-ket' notation, we have for the matrix-operator element

$$\langle n|\hat{J}_x|m\rangle = \int_{-\infty}^{\infty} u_{j,n}^* \hat{J}_x u_{j,m} \, d\tau . \qquad \text{(a-6)}$$

Using the Pauli spin matrices to evaluate the spin components $\hat{J}_x$, $\hat{J}_y$ and $\hat{J}_z$ for a spin 1/2 system where

$$\hat{J}_x = \frac{1}{2}\begin{bmatrix} 0 & 1 \\ 1 & 0 \end{bmatrix}; \quad \hat{J}_y = \frac{1}{2}\begin{bmatrix} 0 & -i \\ i & 0 \end{bmatrix}; \quad \hat{J}_z = \frac{1}{2}\begin{bmatrix} 1 & 0 \\ 0 & -1 \end{bmatrix} , \qquad \text{(a-7)}$$

we see that for $\hat{J}_x$, the matrix elements vanish for m=n. Therefore, m=-n=+1/2 and m=-n=-1/2 which leads to

$$\langle \hat{\mu}_x(t) \rangle = \gamma\hbar \left\{ a^*_{-1/2} a_{1/2} \langle -\tfrac{1}{2} | \hat{J}_x | \tfrac{1}{2} \rangle e^{(i/\hbar)[E_{-1/2} - E_{1/2}]t} \right.$$

$$\left. + a^*_{1/2} a_{-1/2} \langle \tfrac{1}{2} | \hat{J}_x | -\tfrac{1}{2} \rangle e^{(i/\hbar)[E_{1/2} - E_{-1/2}]t} \right\} . \qquad \text{(a-8)}$$

By eq.(3) sec. III, $E_{-1/2} > E_{1/2}$ so $\Delta E = E_{-1/2} - E_{1/2}$ is the Zeeman energy difference between each eigenstate which is simply the transition energy $\gamma\hbar H_o$. (Note that without the applied field $H_o$, the time dependence of $\langle \hat{\mu}_x(t) \rangle$ vanishes.) Substituting $\pm\Delta E = \gamma\hbar H_o$ in eq.(a-8),

$$\langle \hat{\mu}_x(t) \rangle = \gamma\hbar \left\{ a^*_{-1/2} a_{1/2} \langle -\tfrac{1}{2} | \hat{J}_x | \tfrac{1}{2} \rangle e^{(i\gamma H_o t)} \right.$$

$$\left. + a^*_{1/2} a_{-1/2} \langle \tfrac{1}{2} | \hat{J}_x | -\tfrac{1}{2} \rangle e^{-(i\gamma H_o t)} \right\} . \qquad \text{(a-9)}$$

Since in this last expression, $\gamma H_o$ has the units of angular frequency, we may define $\omega_o \equiv \gamma H_o$.

The matrix elements in the Dirac 'bra-ket' notation of eq.(a-9) are complex conjugates; a result of $\hat{J}_x$ being Hermitian:

$$\langle -\tfrac{1}{2} | \hat{J}_x | \tfrac{1}{2} \rangle = \int_{-\infty}^{\infty} u^*_{j,-\frac{1}{2}} \hat{J}_x u_{j,\frac{1}{2}} \, d\tau \, , \qquad \text{(a-10)}$$

$$\langle \tfrac{1}{2} | \hat{J}_x | -\tfrac{1}{2} \rangle = \int_{-\infty}^{\infty} u^*_{j,\frac{1}{2}} \hat{J}_x u_{j,-\frac{1}{2}} \, d\tau .$$

By the definition of Hermitian operators, the right sides of these equations are equal since the eigenfunctions $u_{j,\pm\frac{1}{2}}$ for our system are well behaved functions of position, vanish at infinity, and are real. Therefore, $\langle -\tfrac{1}{2} | \hat{J}_x | \tfrac{1}{2} \rangle = \langle \tfrac{1}{2} | \hat{J}_x | -\tfrac{1}{2} \rangle$ which

when substituted in eq.(a-9) yields

$$\langle \hat{\mu}_x(t) \rangle = 2\pi h \, \mathrm{Re} \left\{ a^*_{+\frac{1}{2}} a_{-\frac{1}{2}} \langle \tfrac{1}{2} | \hat{J}_x | -\tfrac{1}{2} \rangle e^{-(i\omega_0 t)} \right\}. \quad \text{(a-11)}$$

We seek the real part of this equation because the value $\langle \hat{\mu}_x(t) \rangle$ is a real, physical observable.

In order to evaluate the matrix element $\langle 1/2 | \hat{J}_x | -1/2 \rangle$ in eq.(a-11), we need an operator that will transform the ket vector $|m\rangle$ (i.e. the eigenfunction $u_{j,m}$ of $\hat{J}_x$ ) into a new ket vector whose eigenvalue m has been raised or lowered by one unit. To conserve angular momentum, we use the "ladder", or "raising and lowering", operators defined by

$$\begin{aligned} \hat{J}_+ &= \hat{J}_x + i \hat{J}_y , \\ \hat{J}_- &= \hat{J}_x - i \hat{J}_y , \end{aligned} \quad \text{(a-12)}$$

or,

$$\begin{aligned} \hat{J}_x &= \tfrac{1}{2} \left[ \hat{J}_+ + \hat{J}_- \right], \\ \hat{J}_y &= \tfrac{1}{2i} \left[ \hat{J}_+ - \hat{J}_- \right], \end{aligned} \quad \text{(a-13)}$$

where the transformation of the ket vector goes as

$$\begin{aligned} \hat{J}_+ |m\rangle &= \sqrt{(j-m)(j+m+1)}\, |m+1\rangle , \\ \hat{J}_- |m\rangle &= \sqrt{(j+m)(j-m+1)}\, |m-1\rangle . \end{aligned} \quad \text{(a-14)}$$

For spin 1/2 nuclei,

$$\begin{aligned} \hat{J}_+ |-\tfrac{1}{2}\rangle &= \sqrt{(\tfrac{1}{2}+\tfrac{1}{2})(\tfrac{1}{2}-\tfrac{1}{2}+1)}\, |-\tfrac{1}{2}+1\rangle = |+\tfrac{1}{2}\rangle , \\ \hat{J}_- |-\tfrac{1}{2}\rangle &= \sqrt{(\tfrac{1}{2}-\tfrac{1}{2})(\tfrac{1}{2}+\tfrac{1}{2}+1)}\, |-\tfrac{1}{2}-1\rangle = 0 . \end{aligned} \quad \text{(a-15)}$$

These equations must be correct for a spin-1/2 system since in its -1/2 state, it can only be transformed to its +1/2 state, done so by $\hat{J}_+$: $|-1/2\rangle \equiv u_{\frac{1}{2},-\frac{1}{2}} \rightarrow |1/2\rangle \equiv u_{\frac{1}{2},\frac{1}{2}}$.

Therefore, we have

$$\langle \tfrac{1}{2}|\hat{J}_x|-\tfrac{1}{2}\rangle \equiv \int_{-\infty}^{\infty} u^*_{\frac{1}{2},\frac{1}{2}} (\hat{J}_x u_{\frac{1}{2},-\frac{1}{2}})\, d\tau$$

$$= \tfrac{1}{2}\int_{-\infty}^{\infty} u^*_{\frac{1}{2},\frac{1}{2}} \left[\hat{J}_+ + \hat{J}_-\right] u_{\frac{1}{2},-\frac{1}{2}}\, d\tau$$

$$= \frac{1}{2}\int_{-\infty}^{\infty} u^*_{\frac{1}{2},\frac{1}{2}}\, u_{\frac{1}{2},\frac{1}{2}}\, d\tau$$

$$= \frac{1}{2}\,, \qquad \text{(a-16)}$$

where in the final step, we used the eigenvector normalization condition (a property of the Hermitian operator $\hat{J}_x$):

$$\langle n|m\rangle = \int_{-\infty}^{\infty} u^*_{j,n}\, u_{j,m}\, d\tau = \delta_{nm}\,.$$

Finally, the complex constants $a_{1/2}$ and $a_{-1/2}$ in eq.(a-11) in their most general form may contribute both to the phase and amplitude of the wave function. Therefore, we may define

$$a_{1/2} = a e^{i\alpha} \qquad \text{and} \qquad a_{-1/2} = b e^{i\beta} \qquad \text{(a-17)}$$

for a and b real and positive; $\alpha$ and $\beta$ real but positive or negative [10]. Therefore, using Euler's formula, eq.(a-11) becomes

$$\langle \hat{\mu}_x(t) \rangle = \gamma\hbar \, \mathrm{Re}\left[ab e^{i(\beta-\alpha-\omega_0 t)}\right]$$

$$= \gamma\hbar ab \cos(\alpha-\beta+\omega_0 t).$$

(a-18)

The expectation value $\langle \hat{\mu}_y(t) \rangle$ is solved identically to that of $\langle \hat{\mu}_x(t) \rangle$ by starting with eq.(a-5) for $\langle \hat{\mu}_y(t) \rangle$, using the Pauli spin matrix for $\hat{J}_y$ and making the same analysis with the ladder operators in eqs.(a-12,13) which gives

$$\langle \hat{\mu}_y(t) \rangle = -\gamma\hbar ab \sin(\alpha-\beta+\omega_0 t). \qquad \text{(a-19)}$$

The expectation value $\langle \hat{\mu}_z(t) \rangle$ however, has a somewhat preferred orientation since it is parallel to the magnetic field $\vec{H}_0$. Starting with eq.(a-5) for the z-component

$$\langle \hat{\mu}_z(t) \rangle = \sum_{n,m} \gamma\hbar a_n^* a_m \langle n|\hat{J}_z|m\rangle e^{(i/\hbar)[E_n - E_m]t}, \qquad \text{(a-20)}$$

and evaluating the Pauli spin matrix for $\hat{J}_z$, (again for a spin-1/2 system) m = n = $\pm$ 1/2. We see immediately that the time dependent phase factor in eq.(a-20) vanishes leaving

$$\langle \hat{\mu}_z \rangle = \gamma\hbar \sum_{n,m} a_m^* a_m \langle m|\hat{J}_z|m\rangle$$

$$= \gamma\hbar \left[a_{1/2}^* a_{1/2}\left(\tfrac{1}{2}\right) + a_{-1/2}^* a_{-1/2}\left(-\tfrac{1}{2}\right)\right]$$

$$= (\gamma\hbar/2)\left[a_{1/2}^* a_{1/2} - a_{-1/2}^* a_{-1/2}\right]. \qquad \text{(a-21)}$$

Using the constants in eq.(a-17), we find

$$\langle \hat{\mu}_z \rangle = \frac{\gamma \hbar}{2} [a^2 - b^2]. \qquad \text{(a-22)}$$

## APPENDIX B

Time dependent solutions of the Bloch equations for the case of free induction decay in the laboratory and rotating frames:

In the total field $\vec{H} = \vec{H}_0 + \vec{H}_1$, $\vec{H}_1$ should ideally rotate about the z-axis with angular frequency $\omega = \omega_0$ which flips $\vec{M}$ into the x-y plane. Since $H_1$ can only be made to oscillate experimentally, we can remedy the situation by noting, as Bloch did, that an oscillatory field consists of two superimposed fields which rotate in opposite directions. Much of the literature [9] [15] [18] suggests an oscillating field linearly polarized along x as

$$H_x = 2H_1 \cos\omega t \qquad H_y = 0 \qquad H_z = 0 \; . \qquad \text{(b-1)}$$

This field can be decomposed as the sum of two fields rotating about the z-axis in opposite directions where

| Right: | Left: | |
|---|---|---|
| $H_x = H_1 \cos\omega t$ | $H_x = H_1 \cos\omega t$ | |
| $H_y = H_1 \sin\omega t$ | $H_y = -H_1 \sin\omega t$ | (b-2) |
| $H_z = 0$ | $H_z = 0$ | |

The "right" and "left" fields correspond to $+\omega\hat{k}$ and $-\omega\hat{k}$ respectively. At resonance, one of the rotating components in eq.(b-2) will follow $\vec{M}$ while the other will be so far off resonance as

to negligibly effect its motion. Therefore, the oscillating field of eq.(b-1) is quite accurately replaced by either rotating field in eq.(b-2).

Taking $\gamma$ as negative for convenience, we use the "left" rotating field in eq.(b-2) since its rotation in the -z direction is consistent with $\omega_o$ for a $-\gamma$ where $\omega_o = -\gamma H_o$. And, combining $H_o$ we have

$$\begin{aligned} H_x &= H_1 \cos\omega t \ , \\ H_y &= -H_1 \sin\omega t \ , \\ H_z &= H_o \ . \end{aligned} \qquad \text{(b-3)}$$

Upon substitution into the Bloch equations, we find

$$\begin{aligned} dM_x/dt &= \gamma[M_y H_o + M_z H_1 \sin\omega t] - M_x/T_2^* \ , \\ dM_y/dt &= \gamma[M_z H_1 \cos\omega t - M_x H_o] - M_y/T_2^* \ , \\ dM_z/dt &= \gamma[-M_x H_1 \sin\omega t - M_y H_1 \cos\omega t] + \frac{M_o - M_z}{T_1} \ . \end{aligned} \qquad \text{(b-4)}$$

These expressions describe the motion of $\vec{M}$ during the pulse. However, we wish to investigate how $\vec{M}$ behaves during free induction following the pulse. Therefore, eliminating terms involving $H_1$, eqs.(b-4) become

$$dM_x/dt = \gamma M_y H_o - M_x/T_2^* \ , \qquad \text{(b-5)}$$

$$dM_y/dt = -\gamma M_x H_o - M_y/T_2^* \ , \qquad \text{(b-6)}$$

$$dM_z/dt = (M_o - M_z)/T_1 \ . \qquad \text{(b-7)}$$

These equations can be simplified by substituting constants as follows

$$\frac{dM_x}{dt} = aM_y + bM_x \,, \qquad \text{(b-8)}$$

$$\frac{dM_y}{dt} = -aM_x + bM_y \,, \qquad \text{(b-9)}$$

$$\frac{dM_z}{dt} = fM_z + c \,, \qquad \text{(b-10)}$$

where: $a=\gamma H_o$, $b=-1/T_2^*$, $c=M_o/T_1$, and $f=-1/T_1$.

Equations (b-8) and (b-9), due to their symmetry, may be solved by defining the complex numbers,

$$\mathcal{M}_+ = M_x + iM_y \,, \qquad \text{(b-11)}$$

$$\mathcal{M}_- = M_x - iM_y \,, \qquad \text{(b-12)}$$

or,

$$M_x = \tfrac{1}{2}[\mathcal{M}_+ + \mathcal{M}_-] \,, \qquad \text{(b-13)}$$

$$M_y = \tfrac{1}{2i}[\mathcal{M}_+ - \mathcal{M}_-] \,. \qquad \text{(b-14)}$$

By adding i times eq(b-9) to eq.(b-8), then subtracting i times eq.(b-9) from eq.(b-8), we obtain

$$d\mathcal{M}_+/dt = -ai\mathcal{M}_+ + b\mathcal{M}_+ \,, \qquad \text{(b-15)}$$

$$d\mathcal{M}_-/dt = ai\mathcal{M}_- + b\mathcal{M}_- \,. \qquad \text{(b-16)}$$

These equations are easily solved using basic methods:

$$\frac{d\mathcal{M}_+}{dt} = (b-ai)\mathcal{M}_+ \,,$$

$$\ln \mathcal{M}_+ = (b-ai)t + g \,,$$

g=cons't.

$$\mathcal{M}_+ = M_{T_o} e^{(b-ai)t} \,.$$

Here, $M_{T_0}=\exp(g)$. Substituting for the constants a and b,

$$\mathcal{M}_+ = M_{T_0} e^{-t/T_2^*} e^{-\gamma H_0 i t} . \qquad \text{(b-17)}$$

Similarly,

$$\mathcal{M}_- = M'_{T_0} e^{-t/T_2^*} e^{\gamma H_0 i t} . \qquad \text{(b-18)}$$

Using eqs.(b-13) and (b-14), we recover the forms of each component of transverse magnetization

$$M_x = \tfrac{1}{2}\left[M_{T_0} e^{-t/T_2^*} e^{-\gamma H_0 i t} + M'_{T_0} e^{-t/T_2^*} e^{\gamma H_0 i t}\right], \qquad \text{(b-19)}$$

$$M_y = \tfrac{1}{2i}\left[M_{T_0} e^{-t/T_2^*} e^{-\gamma H_0 i t} - M'_{T_0} e^{-t/T_2^*} e^{\gamma H_0 i t}\right]. \qquad \text{(b-20)}$$

We may assume $M_{T_0} = M'_{T_0}$ for isotropic and homogeneous samples. Using this, the relation $\gamma H_0 = \omega_0$, and the identities

$$\cos z = \tfrac{1}{2}\left[e^{iz} + e^{-iz}\right],$$

$$\sin z = \tfrac{1}{2i}\left[e^{iz} - e^{-iz}\right],$$

eqs.(b-19) and (b-20) become

$$M_x = M_{T_0} e^{-t/T_2^*} \cos\omega_0 t , \qquad \text{(b-21)}$$

$$M_y = -M_{T_0} e^{-t/T_2^*} \sin\omega_0 t . \qquad \text{(b-22)}$$

In a frame rotating at $\omega_0$, these equations can be modified by considering the transverse magnetization $\vec{M}_T \left(= \vec{M}_x + \vec{M}_y\right)$ where

$$M_T^2 = M_x^2 + M_y^2,$$

$$= \left(M_{T_0} e^{-t/T_2^*}\right)^2 \left[\cos^2\omega_0 t + \sin^2\omega_0 t\right],$$

$$M_T = M_{T_0} e^{-t/T_2^*},$$

and, $M_{T_0}$ is the initial (t=0) transverse magnetization.

Depending on how $\vec{M}$ falls into the x'-y' plane at t=0, the initial magnitudes of $M_{x'}$ and $M_{y'}$ are related by $\theta$ where

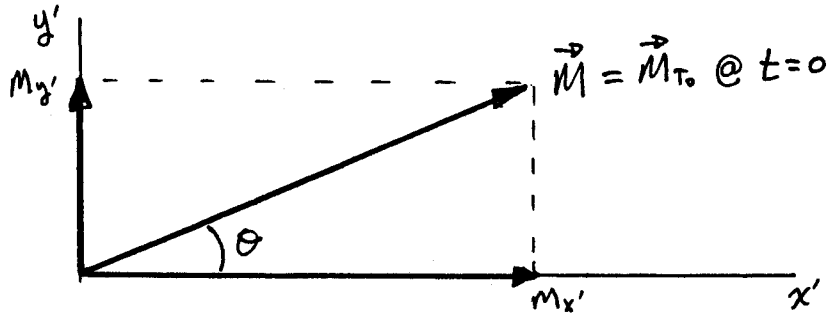


From this geometry,

$$M_{x'} = M_{T_0} \cos\theta\, e^{-t/T_2^*},$$

$$M_{y'} = M_{T_0} \sin\theta\, e^{-t/T_2^*},$$

and setting $M_{0x'} = (\cos\theta) M_{T_0}$ and $M_{0y'} = (\sin\theta) M_{T_0}$ for the initial magnitudes, we have for the rotating frame

$$M_{x'} = M_{0x'} e^{-t/T_2^*}, \qquad \text{(b-23)}$$

$$M_{y'} = M_{0y'} e^{-t/T_2^*}. \qquad \text{(b-24)}$$

The longitudinal magnetization is also solved using basic principles where, again

$$\frac{dM_z}{dt} = fM_z + C, \qquad \text{(b-10)}$$

which takes the form of a first order linear equation, requiring the integrating factor

$$M_z = e^{-\int f dt} = e^{-ft}.$$

Applying this to eq.(b-10),

$$e^{-ft}\left[\frac{dM_z}{dt} - fM_z\right] = e^{-ft}[C],$$

and noting that the left side of this equation is

$$\frac{d}{dt}\left[e^{-ft}M_z\right] = Ce^{-ft},$$

we have, upon integration

$$\int d\left[e^{-ft}M_z\right] = C\int e^{-ft}dt,$$

$$e^{-ft}M_z = -\frac{C}{f}e^{-ft} + A,$$

where A=cons't. Noting that $-c/f=M_o$ and substituting for the remaining constant f, we have

$$e^{t/T_1}M_z = M_o e^{t/T_1} + A.$$

Eliminating $\exp(t/T_1)$, this equation becomes

$$M_z = M_o + Ae^{-t/T_1}.$$

The constant A is easily found for our particular geometry by using the boundary condition: $M_z=0$ at time t=0 immediately following the 90° resonant pulse. Therefore,

$$A = -M_o .$$

Finally, we have the last of Bloch's equations

$$M_z = M_o \left(1 - e^{-t/T_1}\right). \qquad \text{(b-25)}$$